3-21-2019

Computational Aerothermodynamic Analysis of Satellite Trans-Atmospheric Skip Entry Survivability

John J. Runco

COMPUTATIONAL AEROTHERMODYNAMIC ANALYSIS OF SATELLITE TRANS-ATMOSPHERIC SKIP ENTRY SURVIVABILITY

THESIS

John J. Runco, Captain, USAF

AFIT-ENY-MS-19-M-243

DEPARTMENT OF THE AIR FORCE
AIR UNIVERSITY

AIR FORCE INSTITUTE OF TECHNOLOGY

Wright-Patterson Air Force Base, Ohio

The views expressed in this thesis are those of the author and do not reflect the official policy or position of the United States Air Force, the United States Department of Defense or the United States Government. This is an academic work and should not be used to imply or infer actual mission capability or limitations.

AFIT-ENY-MS-19-M-243

COMPUTATIONAL AEROTHERMODYNAMIC ANALYSIS OF SATELLITE TRANS-ATMOSPHERIC SKIP ENTRY SURVIVABILITY

THESIS

Presented to the Faculty

Department of Aeronautics and Astronautics

Graduate School of Engineering and Management

Air Force Institute of Technology

Air University

Air Education and Training Command

in Partial Fulfillment of the Requirements for the

Degree of Master of Science in Aeronautical Engineering

John J. Runco, BS

Captain, USAF

21 March 2019

AFIT-ENY-MS-19-M-243

COMPUTATIONAL AEROTHERMODYNAMIC ANALYSIS OF SATELLITE TRANS-ATMOSPHERIC SKIP ENTRY SURVIVABILITY

John J. Runco, BS
Captain, USAF

Approved:

Maj Robert Bettinger, PhD (Chairman)	Date
Lt Col Jeffrey Komives, PhD (Member)	Date
Lt Col Kirk Johnson, PhD (Member)	Date

Abstract

Reentry is a spacecraft operation that is typically executed as an end-of-life terminal operation. A variation on reentry, called skip entry, is an aeroassisted maneuver in which a spacecraft reenters the Earth's atmosphere, utilizes the effects of aerodynamic drag, and exits thereafter. This can be executed to reduce energy prior to a terminal entry, to pinpoint a targeted entry, or to change orbital elements such as inclination. Examining the skip entry maneuver for a satellite body is a compelling area of research that has yet to be analyzed. A satellite's ability to change orbital inclination with significantly less fuel expenditure would enable new modes of maneuvers in an environment previously avoided. The research presented examines the aerothermodynamic effects of a skip entry trajectory for a small satellite to determine the survivability limits for potential future practical implementation. Can a satellite successfully execute a beneficial skip entry maneuver?

The main assumptions underpinning the analysis include an inertial geocentric equatorial reference frame, an exponential atmosphere model, and an inverse square law of gravity model. Validation of the selected Direct Simulation Monte Carlo (DSMC) solver, SPARTA, was performed using NASA's RAM C-II geometry. The reentry equations of motion, coupled with skip entry non-dimensional equations, were used to determine the perigee velocities corresponding with four perigee altitudes. The current analysis suggests that the satellite skip entry maneuver is feasible at higher depths within the atmosphere. Below a given altitude, the pressure, gravitational, and aerothermodynamic effects become too great for the satellite to overcome. The research presented will discuss the results of the satellite skip entry DSMC computations, with relevant aerothermodynamic data related to skip perigee altitudes and

their corresponding velocities, and it suggests a 90 km skip perigee altitude is feasible for the researched smallsat.

Acknowledgements

I would like to thank Major Robert Bettinger, my thesis advisor, for all the help and support he has provided throughout my research. I would also like to thank Lt Col Jeffrey Komives for sacrificing a considerable amount of time assisting me with the DSMC simulator coding process. In addition, the simulator developers Dr. Steve Plimpton and Dr. Michael Gallis, proposed valuable suggestions to troubleshoot and optimize my code. Other individuals I would like to acknowledge include Dr. Maninder Grover and Dr. Eswar Josyula, for providing insightful knowledge on both DSMC and fluid dynamics. Finally, I would like to thank my mother, father, and brother, for their positive support in the journey to complete my thesis.

John J. Runco

Table of Contents

Page

Page

List of Figures

Figure Page

List of Tables

COMPUTATIONAL AEROTHERMODYNAMIC ANALYSIS OF SATELLITE TRANS-ATMOSPHERIC SKIP ENTRY SURVIVABILITY

I. Introduction

1.1 General Issue

Reentry is a spacecraft operation that is typically executed as a terminal maneuver. This could include the successful landing of manned spaceflight or the deliberate breakup of an unserviceable spacecraft. Another form of reentry, called skip entry, is a transatmospheric aeroassisted maneuver in which a spacecraft reenters the Earth's atmosphere, utilizes the effects of aerodynamic drag, and exits thereafter. This can be executed to reduce energy prior to a terminal entry, to pinpoint a targeted entry, or to change orbital elements such as inclination. In recent decades, the National Aeronautics and Space Administration (NASA) has researched skip entry guidance algorithms for lunar capsule targeted skip entry [7]. Examining the skip entry maneuver for a satellite body is an interesting area of research that has yet to be analyzed. A satellite's ability to change orbital inclination with significantly less fuel expenditure would enable new modes of maneuvers in an environment previously avoided. The research presented in this thesis examines the aerothermodynamic effects of a skip entry trajectory for a small satellite, with the goal to determine the survivability limits for potential future practical implementation.

1.2 Research Objectives

Substantial skip entry research has previously been conducted for spaceplanes and lunar reentry capsules. However, the maneuver has not yet been analyzed specifically for a spacecraft not intended to reenter the atmosphere, hereafter referred to as a "satellite." Overall, this research can be reduced to a single question: Can a satellite survive a skip entry maneuver? To explore this possibility, the research objectives underpinning this research are as follows:

- Validate the use of a Direct Simulation Monte Carlo (DSMC) rarefied flow simulator for satellite analysis.
- Explore perigee depth limitations for a generic satellite structural configuration.
- Compare an established reentry heating model to the the stagnation heat flux and loading effects at various skip perigee altitudes.
- Determine a range of entry flight path angles that yield a corresponding skip perigee within survivable aerothermodynamic limits.

1.3 Methodology

The geometry and dimensions for the generic satellite analyzed in this research is shown by Fig 1. The satellite bus is prismatic in shape and measures (0.7x0.7x0.7) m^3; when deployed, the full length of the solar arrays and bus measures 4 m. The satellite's physical and aerodynamic characteristics are given in Table 1. The drag reference area, S, is based on the body area exposed to the incoming flow and, as a result, will vary based on flight orientation. For an x-z orientation, the drag reference area will simply be the surface area of one side of the cubic frame, 0.49 m^2. An x-y orientation will include the broad-faced area of the solar panels for a total of 2.59 m^2; likewise,

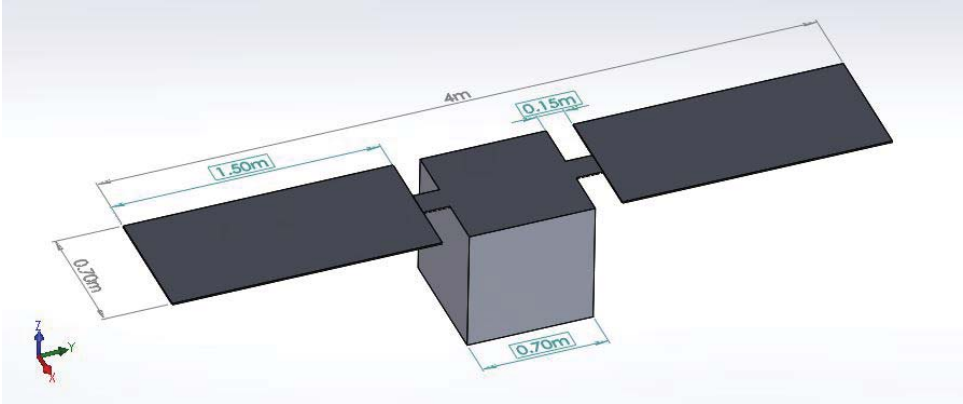

Figure 1. Satellite Dimensions

a y-z orientation will also neglect the solar panels where $S = 0.49$ m^2. Based on a mass of 100 kg, the satellite can be classified as a system between the minisatellite and microsatellite categories [8].

Table 1. Satellite Physical Characteristics

Feature	Value
Length, L	4.0 m
Width, W	0.7 m
Mass, m	100 kg
Reference Area, S	0.49 m^2
Lift Coefficient, C_L	0.4
Drag Coefficient, C_D	2.2

The aerothermodynamic properties will be evaluated using a DSMC simulator. First established by Bird in 1963, DSMC is useful for flow analysis of non-equilibrium gases [9]. Higher within the atmosphere, rarefied air is less dense and, therefore, the collision of particles over hypersonic geometries is typically binary. Binary collisions are characteristics of dilute gases, which generally encompass the majority of DSMC analysis. This is in comparison to a dense gas, which involves numerous molecules

per collision. A dilute gas' average molecule diameter is significantly smaller than the mean separation distance between molecules; as a gas becomes more dense, the length difference becomes minimal. A larger diameter to separation distance ratio equates to a more dense gas. It is important to note that many dilute gas environments still require continuum simulations [9].

Another DSMC factor to consider is the fluctuation of gas properties, specifically the changes in density, pressure, and temperature. When limited particles in the volume of interest contact the characteristic length[1], the fluctuations in the gas become relevant influencing particles in both time and space. Gas fluctuation relevance is nearly exclusive to free molecular flow, as well as the transition region between continuum and free molecular flow. Both of these scenarios require DSMC simulations, as continuum flow computational fluid dynamics (CFD) cannot accurately calculate these flow properties [9].

The Knudsen number is an effective means for choosing DSMC or CFD to compute flow characteristics:

$$Kn = \frac{\lambda}{L} \tag{1.1}$$

where λ is the mean free path and L is the characteristic length. The mean free path is the average distance between particle collisions, while the characteristic length is arbitrary based on the geometry of interest. If the Knudsen number is greater than 0.01, it can be assumed the continuum flow assumption is no longer valid. This delineation is based on particles experiencing 100 collisions or less over the characteristic length, which is more likely to occur at higher altitudes where atmospheric gas is less dense. It can also occur in a dense region where the characteristic length of a body is extremely small, where the number of collisions still may not exceed the 100-particle threshold. For this scenario, DSMC simulations would still take precedence

[1]The characteristic length is arbitrary for a given geometry and is chosen based on the distance that significantly interacts with the flow, thereby helping define flow properties.

over continuum analysis for optimal accuracy. For $Kn > 10$, this region is considered free molecular flow, where the number of collisions per characteristic length is well below 100. The Knudsen range in between continuum flow and free molecular flow is called the transition region, where Kn $\in [.01, 10]$ [9]. Boyd states that DSMC flow analysis is well-suited for aircraft and spacecraft at high altitudes [9]. The skip entry of a satellite is deemed a proper scenario for the use of DSMC because the perigee altitude analysis range is $h \in [90, 120]$ km, and the Knudsen number for the given altitude range is Kn $\in [0.03, 5.14]$. This Knudsen number range is above the 0.01 threshold where continuum analysis fails and DSMC analysis becomes necessary.

A number of available DSMC flow solvers are computationally accurate within generally accepted tolerances. The simulator selected for this research was the Stochastic PArallel Rarefied-gas Time-accurate Analyzer (SPARTA), which is capable of performing computations in low density regions for flow over 2D or 3D geometries. SPARTA is an open source code which was developed at Sandia National Laboratories [10]. The code continues to be updated; as a result, this research uses the version released on 23 December 2017.

The reentry equations of motion will be used to estimate perigee speeds for the skip trajectories. This will be accomplished by executing a Hohmann transfer[2] from low Earth orbit and excuting a subsequent skip maneuver at an entry interface of 120 km. These perigee speeds are necessary input parameters for SPARTA's DSMC simulator to accurately compute the aerothermodynamic parameters of the satellite.

[2]A Hohmann transfer is a planar maneuver executed to transition from one circular orbit to another; it is fuel efficient, yet generally requires a greater time-of-flight than similar maneuvers [11].

1.4 Preview

Chapter I described the thesis main objectives and presented an overview of the analysis methodology. In Chapter II, a review of the relevant literature will highlight research that has been accomplished in the field of skip entry. This chapter will also discuss previously developed skip entry guidance algorithms, as well as review aerothermodynamic DSMC analysis of select rarefied flow reentry scenarios. Chapter III will provide a more detailed presentation of the methodology, to include the research assumptions and limitations, and the supporting gravity and atmospheric models. The DSMC method's computational analysis process will be discussed based on SPARTA verification of experimental reentry data. In Chapter IV, results of satellite skip entry DSMC computations will be presented, with relevant aerothermodynamic data related to skip perigee altitudes and their corresponding velocities. The last chapter will present the thesis research conclusions and significance, and provide recommendations for future skip entry research.

II. Literature Review

2.1 Chapter Overview

A summary of relevant literature will be reviewed in this chapter including skip entry maneuver specifications, reentry guidance algorithms, and DSMC aerothermodynamic analysis. Numerous DSMC examples will be presented and compared to experimental data, and SPARTA computational results will also be discussed as well.

2.2 Skip Entry

2.2.1 Guidance Algorithm

Skip entry guidance algorithms have been developed by researchers in organizations such as San Diego State University, University of California Davis, and NASA's Johnson Space Center. The University of California Davis executed an analytic skip entry drag profile derivation for typical low lift-to-drag reentry vehicles. By means of DSMC, future plans will determine the analytic algorithm's robustness in using the Simulation of Rocket Trajectories (SORT) program. An analytic guidance code was deemed necessary for a skip-to-touchdown scenario because the current algorithm's computational accuracy is limited to the initial portion of the skip, to include atmospheric entry and exit. In addition, D'Souza examined a minimum g optimization simulation of the low L/D Orion spacecraft in response to excessive g-load and minimal maneuverability concerns; the results determined a maximum horizontal skip entry distance of 8371 km (4520 nautical miles), shown in Fig. 2. Point A is the entry interface, where the spacecraft re-enters the atmosphere, a generally accepted altitude of 120 km. Point B is the perigee altitude, the closest orbital distance to Earth, while the furthest orbital altitude is the apogee altitude at Point C. Briefly entering the atmosphere decreases the spaceccraft's energy, reducing its overall velocity as well.

Multiple skips are feasible before the reduction in energy is high enough that the spacecraft can no longer sustain its orbit. In this scenario, a terminal landing reentry trajectory is ensured unless a burn is executed exoatmospherically to maintain orbital velocity. In Fig. 3, only one skip is executed and Point D illustrates the spacecraft's final trajectory descent to Earth [1].

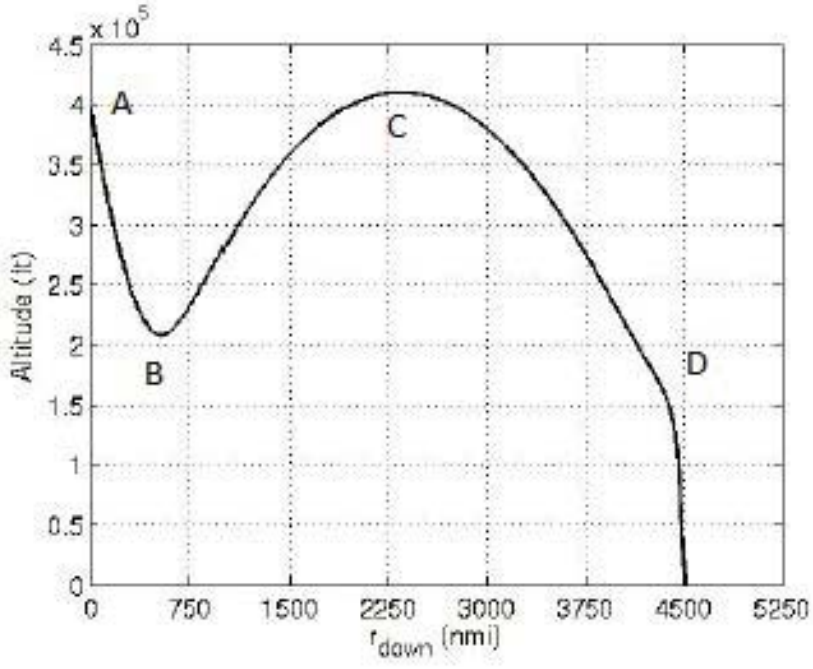

Figure 2. Orion Skip Entry Downrange Distance [1]

A research paper by Lu describes an enhanced entry algorithm in-development called the Fully Numeric-Predictor Entry Guidance (FNPEG), which provides direct and skip entry guidance for numerous vehicle geometries. Testing of FNPEG's algorithm is being executed on NASA's Orion spacecraft at the Johnson Space Center, which currently employs the reentry guidance algorithm PredGuid[1]. One PredGuid drawback is its difficulty executing all phases trajectories, like skip to final-phase. The skip phase includes the initial descent and ascent within the atmosphere, followed by an intermediate exoatmospheric phase, while the final phase consists of a second reen-

[1]PredGuid is Orion's current cutting-edge dual guidance algorithm based on Apollo phase programming, currently being used for comparison with FNPEG [2].

try to landing scenario; these phases are reiterated, and shown more clearly in Fig. 3. By comparison to PredGuid, the FNPEG algorithm does not require a specific trajec-

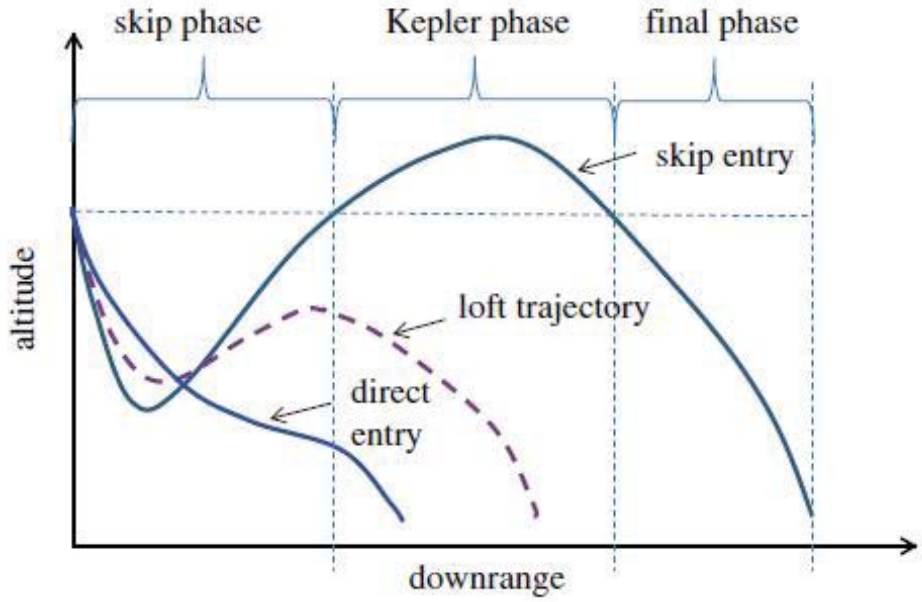

Figure 3. Three Phases of a Terminal Skip Trajectory [2]

tory in order to successfully guide a reentry spacecraft. FNPEG has the potential to measure temperatures and aerothermal loads using Advanced NASA Technology for Architecture and Exploration Studies (ANTARES), which is FNPEG's Monte Carlo simulation environment. Although maintaining great potential, the overall guidance algorithm is still currently in development [2].

2.2.2 Maneuver-Based Specifications

When assessing the extent of research regarding aeroassisted trans-atmospheric responsive skip entry, Bettinger's research provides valuable insight, as his work introduces orbital inclination changes through the execution of the maneuver. This represents an alternate option to the traditional exo-atmospheric burn and, in many scenarios, is an advantageous option for fuel saving. Specifically, skip entry maneuvers

were shown to require a lower ΔV than exo-atmospheric maneuvers when overflying geographically diverse ground targets. The skip entry maneuver was analyzed for a spacecraft with L/D = 6 and bank angle $\sigma = 90°$, so as to achieve a maximum inclination change for a given initial orbital path. Overall, all simulated maneuvers experienced less than a 1 g deceleration force and 1000 kW/m^3 stagnation heat flux. Equation (2.1) provides a closed-form reentry stagnation heat flux approximation:

$$\dot{Q}_S = 199,830 \left(\frac{\rho}{\rho_{SL}}\right)^{0.5} \left(\frac{V_R}{V_{SL}}\right)^{3.15} \frac{kW}{m^2} \tag{2.1}$$

where $V_{SL} = \sqrt{\mu/R_\oplus}$, Earth's gravitational parameter $\mu = 398600.442\ km^3/s^2$, the density at sea level $\rho_{SL} = 1.225$ kg/m^3, and V_R equal to the velocity relative to Earth. Radiative heat flux was neglected for the analysis, because it begins to dominate stagnation heat flux at velocities in excess of 11.2 km/s, which is greater than what will be experienced by a spacecraft during skip entry. The closed form stagnation heat flux in Eq. (2.1) was also used by Darby for small spacecraft orbital transfer maneuvers; it will be utilized for the satellite skip entry DSMC analysis as well [12, 13].

2.3 DSMC

2.3.1 SPARTA

The stochastic analyzer SPARTA has been utilized as a DSMC simulator for multiple areas of research. For example, it has been compared to experimental wind tunnel data by Klothakis for a 70° blunt cone probe and a 25°-55° biconic. The Mars Probe Blunt Cone Geometry figure in [14] illustrates the configuration of the probe that contained the Mars Pathfinder, which reentered Mars' atmosphere in July 1997 [15]. The aforementioned geometry was subject to a wind tunnel environment

and results were compared to different DSMC solvers' simulations. During testing, thermocouple measurements were collected at various S/R_N locations, where S is the distance along the body and R_N is the nose radius. The Mars Probe Contour Velocity Profile figure in [14] shows the velocity magnitude, with flow separation beginning to occur between thermocouples 4 and 5 (S/R_N ~2), where DSMC heat flux computations are generally higher than experimental data [14]. This phenomena is shown in the Mars Probe Surface Heat Flux figure in [14], where the heat flux experimental data points match well with the DSMC profile, with the exception of the body surface at S/$R_N \in [2.2, 4.3]$. This discrepancy is due to the complex flow field and the charged chemical reactions occurring in the low density non-equilibrium flow separation region [16]. The 50-300% error in this region amongst the data for all considered DSMC solvers' simulations led to careful consideration for the selected thermal protection system used in the overall probe design [14].

DSMC simulations were also run for a 25°-55° biconic geometry. SPARTA's ability to determine heat flux values was excellent as compared to experimental data, with the plot of the Biconic figure of SPARTA versus Experimental Data in [14] illustrating 96% of experimental data points being within 10 kW/m^2. The pressure profile illustrates 65% of the experimental data points are within 40 N/m^2 of the SPARTA profile, while 93% of the points are within 80 N/m^2 [14].

2.3.2 Cartesian Grid Cut-Cell Algorithms

A demonstration of DSMC's capacity to accurately simulate reentering spacecraft is further clarified in Zhang's research, which included analysis on a planetary probe and the MIR Space Station. For all analysis, Zhang used MGDS, which is a cut-cell DSMC flow solver developed by Schwartzentruber. Complex surface geometries can be simulated by this algorithm since it creates cells along the body that accurately

capture the flow properties. Cut-cell solvers determine cut-cell volumes, account for split cells[2], and ensure the grid cells adjacent to the geometry all correspond with the correct triangular surface components. Cut-cells can be accurately simulated using your typical DSMC indirect method, while split cell computations require a direct method.

The planetary probe simulation demonstrates the cut-cell algorithm's ability to accurately compute terminal reentry scenarios. The simulation was run for a terminal trajectory at $h = 85$ km and $V = 1502$ m/s; of 622,000 total grid cells, 15 were split-cells and 83,000 were cut-cells. This illustrates the algorithm's ability to accurately simulate an intricate grid mesh to include split cells adjacent to the surface geometry. The accuracy of the method is illustrated in Fig. 4, as the heat flux simulation matches closely with experimental data, with the largest data point error deviation being 7.4%. The probe's grid and surface contours for translational temperature and heat transfer coefficient is shown by Fig. 5, with the grid appropriately well-refined closer to the geometry surface [3].

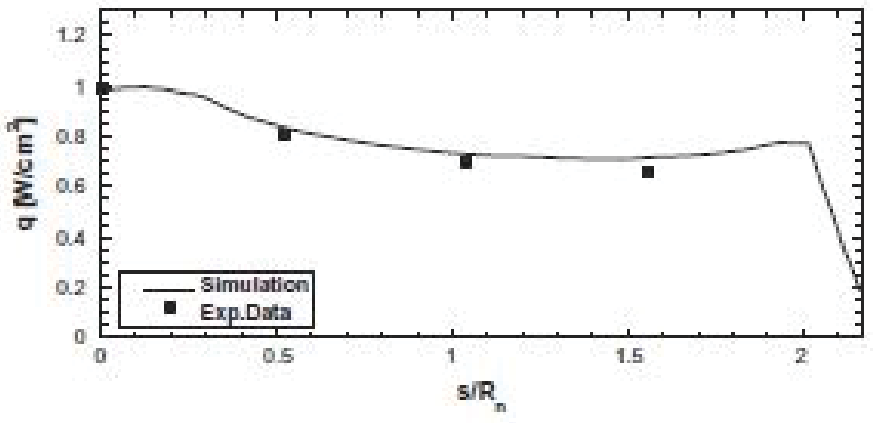

Figure 4. Planetary Probe Heat Flux Profile [3]

[2]Split cells are Cartesian grid cells adjacent to the body surface that are divided into multiple independent polyhedron regions due to the body's usually irregular geometry [3]

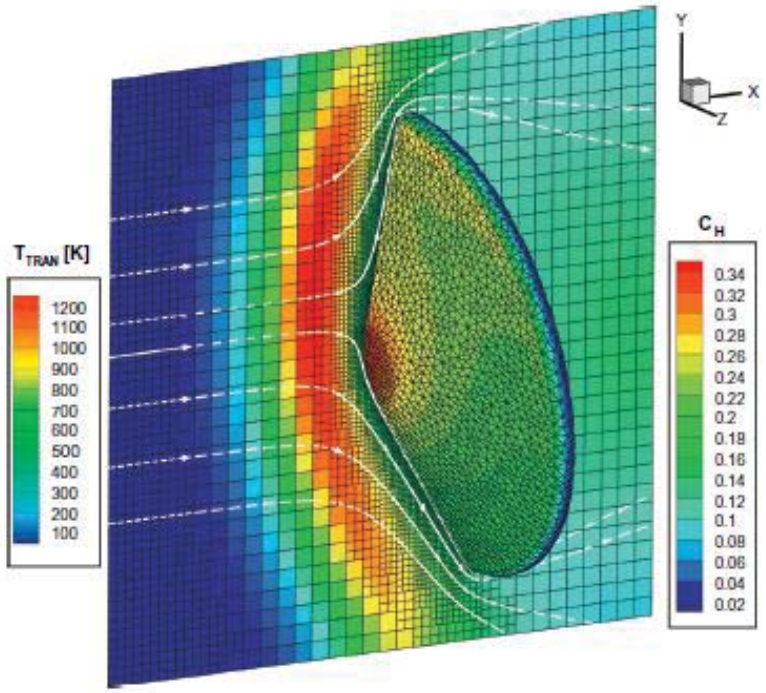

Figure 5. Planetary Probe Grid: Heat Transfer Coefficient and Temperature [3]

End-of-life reentry simulations for MIR Space Station's intricate geometry were executed at an altitude of approximately 115 km. Figure 6 illustrates the ability of the solver to successfully refine and simulate grid and surface parameters close to the body's complex surface. By comparison to the planetary probe, 57,300 of 624,000 total grid cells were cut-cells, while 5,572 were split-cells. The MIR's multifaceted geometry accounts for the greater split cell count at 0.9% compared to the planetary probe at 0.002%. The heat flux contours in Fig. 6 are continuous, showing that the cut-cell algorithm did not negatively affect the output. No experimental data was captured at this altitude for comparison, but the results are promising due to the accuracy of the coding algorithm. The MGDS solver discussed in Zhang's research modifies the surface mesh infrequently in a simulation, saving potential computation time as well [3].

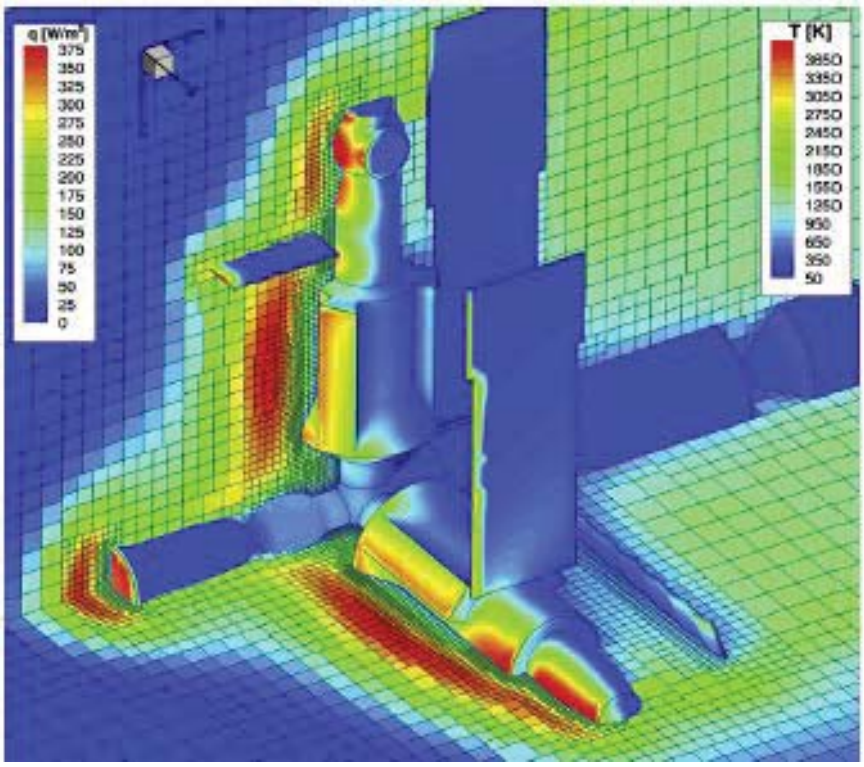

Figure 6. MIR Space Station: Heat Flux and Temperature [3]

2.3.3 DSMC Analysis Code (DAC)

NASA's premier 2001 DSMC Analysis Code, DAC, was used to simulate spacecraft in orbit and during reentry for both Earth and Mars atmospheres [17]. A few of these spacecraft included the MIR Space Station, X-38, Mars Global Surveyor, and the Hubble Space Telescope. Figures 7, 8, 9, and 10 illustrate the profile contours of various DSMC computational parameters. However, they are without accompanying data values, as the paper was emphasizing the variety of complex geometries with which DAC analysis proved to be useful. In-depth data can be found in the references of LeBeau's research paper [4].

A few of the DSMC scenarios will be discussed to highlight DAC's capabilites. The first examined analysis case is the MIR Space Station, whose pressure contours in Fig. 7 actually resulted from the effects of STS-74's reaction control thrusters dur-

ing rendezvous. Another DAC analysis was conducted on the X-38 to predict the

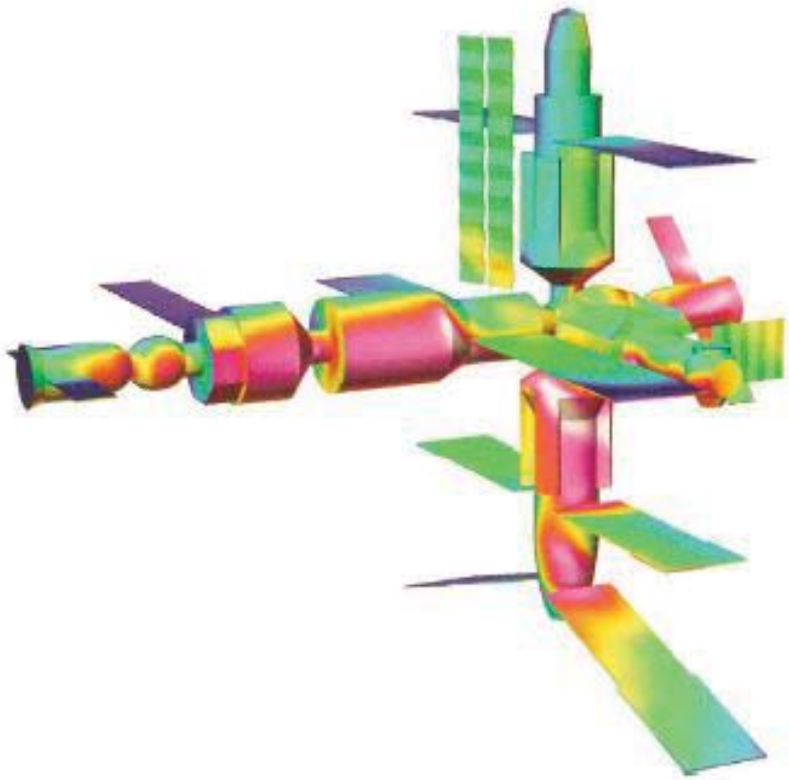

Figure 7. MIR Space Station Surface Pressures [4]

aerodynamics of the spacecraft during reentry. Although conducted prior to the program's cancellation, the simulation results still provide valuable insight into terminal reentry simulations from rarefied air into the transition region between rarefied and continuum flow. The analysis was conducted for $h \in [92, 122]$ km, and the surface pressures are illustrated in Fig. 8. The Mars Global Surveyor Vehicle was a spacecraft of interest as well, considering it observed the planet's surface in orbit and assisted with potential reentry sites for future missions. At one point along its orbital path, the solar panel mechanism malfunctioned inhibiting full extension, and further DSMC analysis was required to calculate the aerothermal values for the previously unanticipated geometry. The modified geometry's surface temperature contours are given in

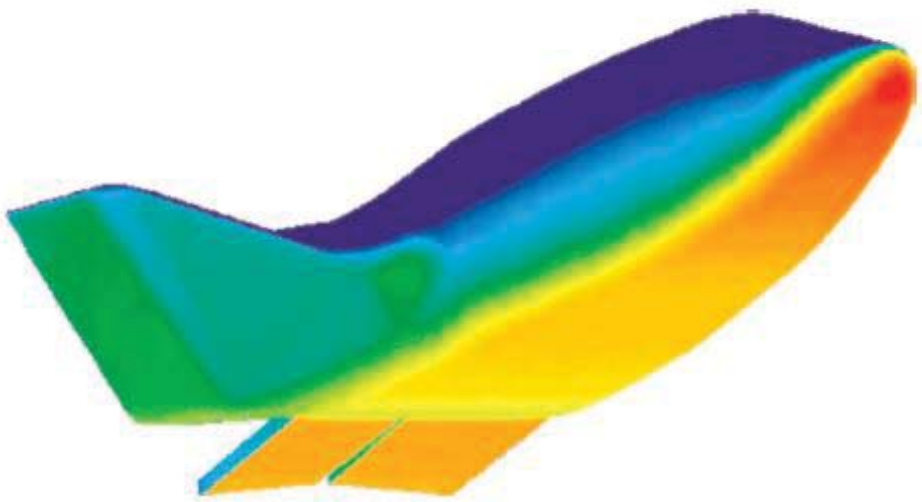

Figure 8. X-38 Surface Pressures [4]

Fig. 9, with computations being executed by the aforementioned DAC. In addition,

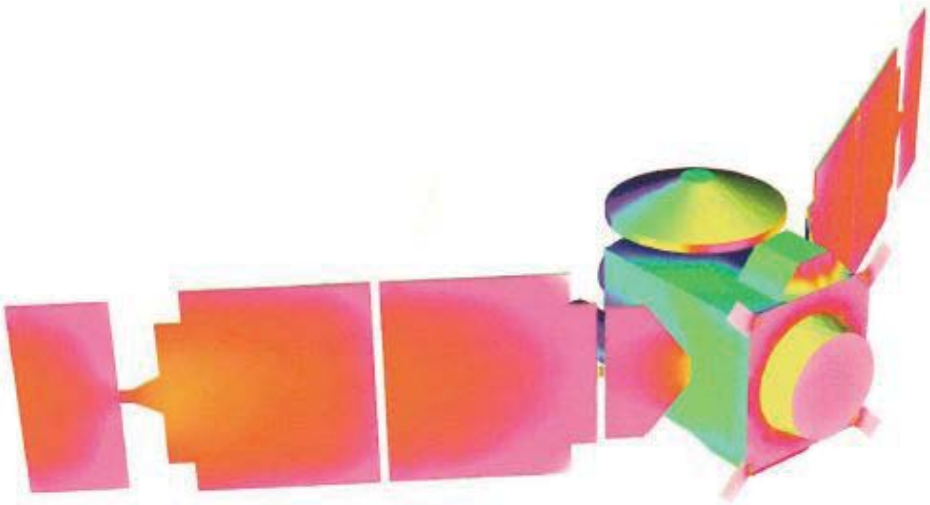

Figure 9. Mars Global Surveyor Surface Heat Diffusion [4]

the Hubble Space Telescope was simulated by NASA's DSMC solver. While being serviced by the STS-82, a vent on the Discovery caused unexpected airflow to rotate one of Hubble's solar arrays 140°, causing a 2-hour delay in servicing. This prompted preventative measures for future missions, in addition to the execution of a DSMC

simulation of the airflow that contacted Hubble's body; the pressures exerted on the telescope are given in Fig. 10 [4, 18].

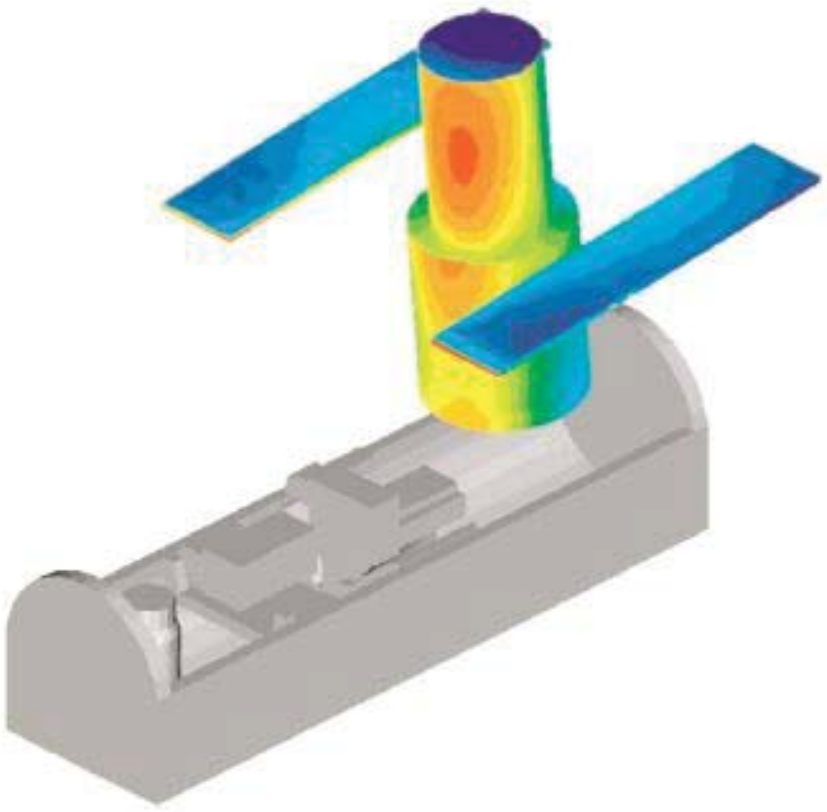

Figure 10. Hubble Space Telescope Pressure Contours [4]

2.4 Summary

A review of relevant skip entry maneuver specifications and DSMC space and reentry analysis was presented in this chapter. DSMC algorithms have proven to be a valuable asset for the study of spacecraft in free molecular flow. Computational aerothermodynamic parameters for numerous orbiting and terminal entry scenarios have provided insightful data, influencing geometries, materials, and thermal protection systems of various spacecraft. NASA's DSMC solver has performed analysis on spacecraft like the MIR Space Station and the Hubble Space telescope. For Mars

reentry and orbiter missions, DSMC has played a vital role in predicting spacecraft aerothermodynamics as well. In addition, SPARTA's DSMC analysis was shown to match well with experimental data, with minor flaws common amongst current DSMC solvers. The previously accomplished DSMC research, however, has only applied to terminal reentry scenarios or orbiting spacecraft. DSMC analysis for skip entry spacecraft is a new area of research that could illuminate potential advantages and drawbacks of attempting this maneuver. The upcoming chapters investigate this possibility for a small satellite.

III. Methodology

3.1 Chapter Overview

This chapter will discuss the methodology used to verify all necessary models, codes, and solvers in this research, to include all assumptions and limitations underpinning the analysis. Validation of the selected DSMC solver, SPARTA, will be performed using the RAM C-II geometry. Finally, the skip reentry equations of motion will be used to determine perigee speeds for subsequent SPARTA simulations.

3.2 Direct Simulation Monte Carlo

In order to validate the use of SPARTA for subsequent satellite analysis, the results of recorded experimental data in a relevant environment were analyzed. A commonly used verification example for CFD and DSMC is that of the RAM C-II, shown in Fig. 11.

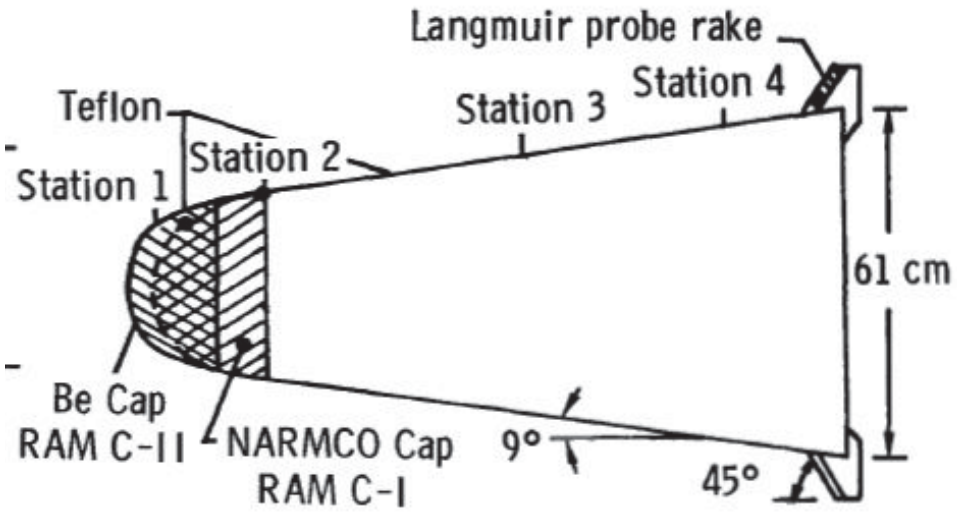

Figure 11. RAM C-II Geometry and Reflectometer Locations [5]

The RAM C-II was a NASA mission researching the "blackout" event that reentry vehicles experience when ionization reactions occur, resulting in a brief interruption of radio signals and loss of communication. The mission was fittingly named Radio Attenuation Measurements (RAM), and consisted of a blunt vehicle with a 9°-spherical nose-cone body. The vehicle was launched on a sub-orbital trajectory and various parameters were measured upon reentry at altitudes of 61, 71, and 81 km [5]. The RAM C-I and RAM C-II experiments were similar reentry tests with slight differences in geometry and mass of the vehicles. The purpose of the RAM C-I experiment was to test water cooling techniques in an effort to reduce or eliminate the blackout event, while the goal of the RAM C-II experiment was to measure electron densities at various locations along the body. Stations 1-4 shown in Fig. 11 represent the sensor locations for all RAM C variants [19].

The RAM C-II's Knudsen number at 81 km was calculated to be 0.016. Recalling that DSMC analysis is valid for $Kn > 0.01$, it is apparent that the experiment is near continuum flow. To reiterate previously mentioned concepts, the transition region between continuum and free molecular flow falls within the range $Kn \in [.01, 10]$; free molecular flow is implied at $Kn > 10$. The Knudsen value of 0.016 warrants the use of DSMC simulations, and SPARTA will be implemented to replicate the RAM C-II data, specifically the electron density at an altitude of 81 km.

3.2.1 Model Parameters

The chemical species in air include nitrogen, oxygen, argon, carbon dioxide, and small percentages of other gases. The 0.93% argon and 0.03% carbon dioxide can be neglected for this analysis [20]. As the RAM C-II enters the atmosphere at hypersonic velocities, kinetic energy thresholds are exceeded and chemical reactions result. These reactions produce additional species including N, O, $N^+, O^+, N2^+, O2^+$, NO, NO^+,

and e^-. The ions $N^+, O^+, N2^+, O2^+$ will have negligible effects on electron number density measurements, because NO^+ is included in the ionization reaction generating the overwhelming majority of free electrons, given by Eq. (3.1) featuring a reaction energy of 63.65 kcal/mol. By comparison, the ionization reaction energies of Eqs. (3.2) and (3.3) are 160.29 kcal/mol and 134.22 kcal/mol, respectively [21]. Upon reentry, the reaction expressed by Eq. (3.1) will occur prior to and more frequently than the latter two reactions. Therefore, the DSMC simulation performed for RAM C-II and subsequent satellite analysis will only use a 7-species model with N2, O2, N, O, NO, NO^+, e^-. All given chemical reactions used the Arrhenius form of the rate equation.

$$N + O \rightarrow NO^+ + e^- \tag{3.1}$$

$$O + O \rightarrow O2^+ + e^- \tag{3.2}$$

$$N + N \rightarrow N2^+ + e^- \tag{3.3}$$

The inverse reactions, or recombination reactions, are also relevant to the analysis:

$$NO^+ + e^- \rightarrow N + O \tag{3.4}$$

$$O2^+ + e^- \rightarrow O + O \tag{3.5}$$

$$N2^+ + e^- \rightarrow N + N \tag{3.6}$$

Though these reactions are pertinent to electron density measurements, they are not currently supported by SPARTA when the ambipolar[1] approximation is simulated. Although this approximation is not essential, its inclusion should enhance the ac-

[1]The term "ambipolar" refers to ambipolar diffusion, or the diffusion of species with opposing charges. When simulated in SPARTA, the electron moves paired with its ion to maintain a neutral electric field [22, 23].

curacy of computed electron densities in a DSMC simulation [24]. This assessment is based on an electron's mass being five orders of magnitude less than all other mentioned species. Therefore, electron velocities will be about three orders of magnitude greater than any ion velocities [24]. Since positively charged ions build up at the surface, the attraction between $NO+$ and e^- hinders electron transport [25]. The ambipolar approximation creates a neutral field around the vehicle body, thus creating a computationally efficient simulation environment that more accurately approximates electron densities [23]. In other words, the ion and electron particles are coupled and move at the same velocity. This prevents a charged electric field from developing around the body [25]. Simulations were run both with and without the ambipolar approximation, and the results and comparison to the experimental data is presented in the upcoming paragraphs.

An additional challenge that DSMC simulations encounter with chemically-charged reactions is the accuracy of collision rates. The probability of a collision occurring is based on the *relative* velocity g and collisional cross section σ between particles. The electron's small mass again creates a challenging problem for these simulations. Recalling the electron's velocity is significantly higher, it will therefore experience collisions much more frequently than other species [24]. To accurately capture these collisions, the timestep must be reduced to an extremely small value. This will increase the computational load to an extent that may not be suitable for the some computer processing capabilities.

For the RAM C-II analysis, the simulation timestep was chosen based on the mean collision time, τ, of the freestream species N2 and O2. The mean collision time τ was calculated to be on the order of 10^{-6}, which prompted a timestep selection of 10^{-7} in order to accurately capture collisions. This is a feasible Δt for the analysis; however, as high-velocity free electrons begin to populate the shock region, the mean collision

time significantly drops. A Δt of 10^{-7} is now too high to accurately capture collisions. Adjusting this timestep to account for electron collisions would require extraordinary computing capabilities. Although one option exists to set different timesteps for different species, this introduces a number of other computing complications [26].

To resolve the timestep issue, the electron mass can be increased three orders of magnitude for simulation purposes only. This surprisingly has negligible effects on electron density computations with the ambipolar approximation. The electron temperatures, however, are affected by this increase in mass. Fortunately, this temperature offset does not affect electron density computations, because the ambipolar setting forces ions and electrons to diffuse together regardless of mass. This adjustment decreases the computational load and is an effective modification to the input parameters for the RAM C-II experiment's electron density analysis [24]. Overall, a simulation electron mass of 9.11 x 10^{-28} amu was programmed instead of a realistic electron mass of 9.11 x 10^{-31} amu.

The ratio of physical particles to simulation particles is also an important DSMC programming parameter. The SPARTA variable designation for this ratio is $fnum$, and the value was chosen based on the order of magnitude resolution that is necessary to accurately simulate electron densities. With the collected experimental data as low as 8.85 x 10^{15} m^{-3}, at attempt was made to reduce $fnum$ below this value so as to ensure the lowest data value is properly captured. However, the simulation encountered memory issues when attempting to run analysis with such a small particle ratio as compared to the freestream number density. With a number density of 3.52 x 10^{20} at 81 km, decreasing the $fnum$ value by any additional order of magnitude increases the number of simulation entry particles by the same magnitude. Hence, memory issues can quickly become problematic. Simulation attempts with an $fnum$

as low as 2.52 x 10^{16} encountered memory issues as well, and a particle ratio of 3.52 x 10^{16} was selected.

3.2.2 Verification

3.2.2.1 Electron Number Density

For the RAM C-II vehicle, electrostatic probe rakes, with the assistance of reflectometer antennas at varying locations, measured the maximum electron densities normal to the vehicle surface during reentry [19]. A visualization of SPARTA electron densities are illustrated in Fig. 12 for the RAM C-II at an altitude of 81 km, and a comparison of the computational and experimental results are shown in Fig. 13. In terms of data collection, the reflectometer antenna locations are specified in Table 2 for both the physical RAM C-II body and the SPARTA model.

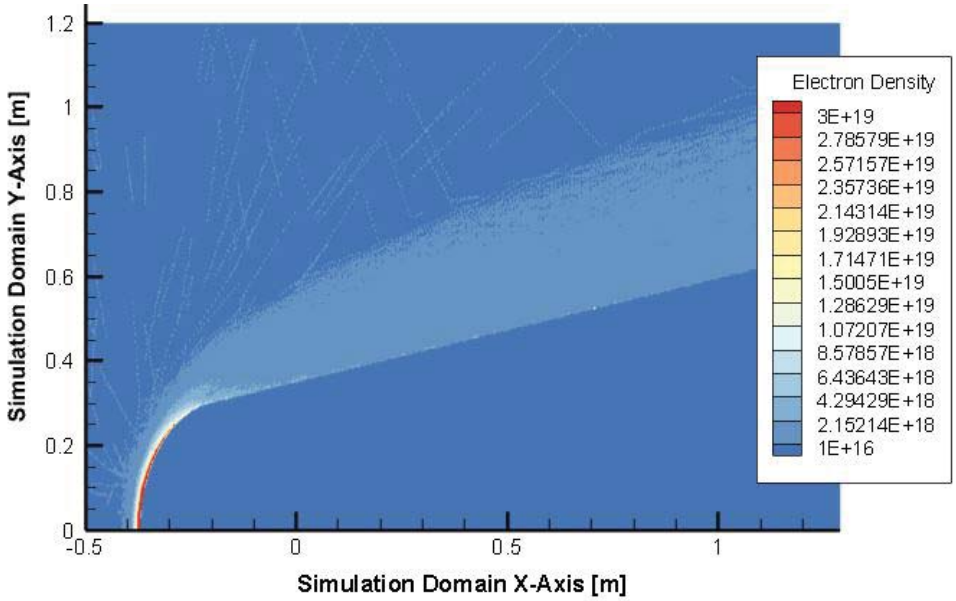

Figure 12. Electron Density Visualization (h=81 km)

On average, the ambipolar approximation simulation differs with the experimental data by about 1.8 orders of magnitude. Since SPARTA does not currently support recombination reactions when the ambipolar approximation is set, this represents

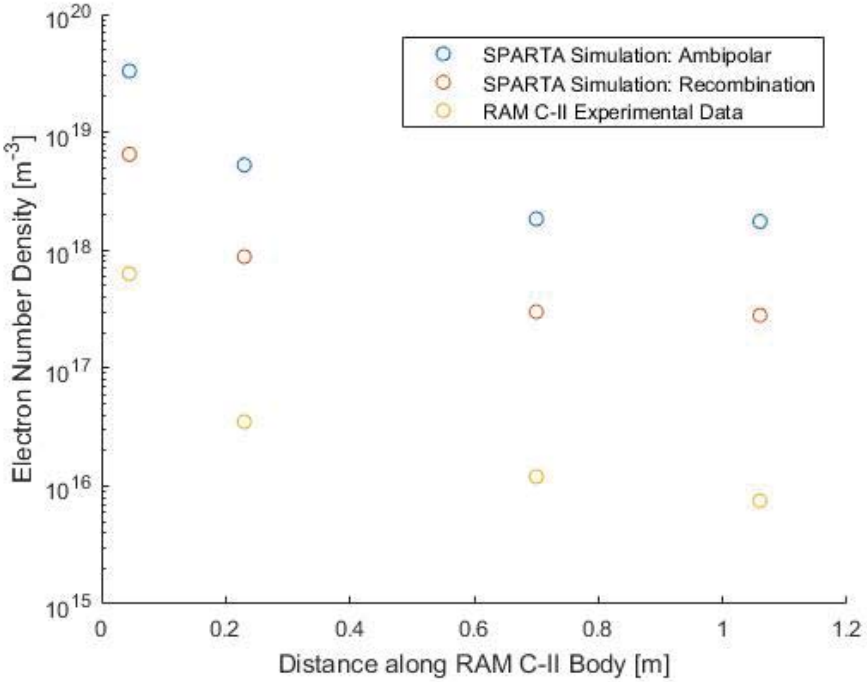

Figure 13. Electron Densities: DSMC vs Experimental Data

one likely explanation for the variation. The relevant recombination reaction from the 7-species model is given by Eq. (3.4), written again for convenience.

$$NO^+ + e^- \rightarrow N + O \tag{3.4}$$

It is worth mentioning that there are typically very few recombination reactions in rarefied air, considering they require 3-body collisions [27]. Binary collisions overwhelm-

Table 2. RAM C-II Reflectometer Antenna Locations

Station	Distance Along RAM C-II Body	Simulation Domain X-Axis Location
1	0.045 m	-0.325 m
2	0.23 m	-0.14 m
3	0.61 m	0.33 m
4	0.70 m	0.69 m

ingly dominate at higher altitudes due to decreasing number densities. However, the current 81 km RAM C-II analysis borders continuum flow with a $Kn = 0.016$, suggesting that recombination reactions would be relevant. A separate simulation was run with recombination manually included into the SPARTA run script, but without the ambipolar approximation set. This simulation is represented by the middle trend of data in Fig. 13 and is labeled "SPARTA Simulation: Recombination." Though these results are closer to the experimental data, the underlying computations do not account for the ambipolar approximation. If the ambipolar simulation could be run with recombination reactions, it is more likely that the error deviation between computational and experimental data would further decrease.

The two SPARTA simulations with and without recombination have nearly identical number density variation trends from station to station. The experimental results do show a greater reduction in electron density from Station 1 to Station 2, with an observed decrease of over one order of magnitude, while the simulations decrease by approximately 0.75 order of magnitude. From Station 2 to Station 3, the electron density fluctuation is nearly consistent across the all data sets. Finally, the reduction in number density from Station 3 to Station 4 is somewhat larger than the SPARTA simulation. The experimental data decreases by approximately 0.4 order of magnitude, while the SPARTA simulations decrease minimally at 0.01 order of magnitude. If SPARTA supported ambipolar recombination, then any error deviations may be resolved.

An interesting consideration is that electron number densities are quite sensitive to the freestream density. For example, a change in freestream density by a factor of 3.6, or an 8 km altitude difference, alters the electron number density by about two orders of magnitude [28]. Densities at specific altitudes also fluctuate based on numerous factors including solar activity. The 1976 U.S. Standard Atmosphere was

referenced to find an appropriate density corresponding to 81 km. Overall, the general data *trend* from one reflectometer to the next does match relatively well across the two SPARTA simulation runs.

3.2.2.2 Stagnation Streamline Temperatures

The temperature contours and stagnation streamline profiles of the RAM C-II can be investigated in addition to the electron density using SPARTA. A select number of published DSMC research also performed this temperature analysis for various vehicles [24, 28]. Figure 14 gives SPARTA translational temperature contours over the RAM C-II geometry: these results match Boyd's analysis with minimal deviation. Figure 15 shows Boyd, Shevyrin, and SPARTA profiles represented by dashed, dotted, and solid lines, respectively. Translational, rotational, and vibrational temperatures are represented by red, green, and blue profiles, respectively. The stagnation lines extends into the freestream region, where the temperature remains steady at a set value of 193 K. The RAM C-II geometry begins at $x/R_N = 0$, where the profiles should converge to the 1000 K surface temperature.

Considering temperature is a quantitative measure of energy, a rudimentary discussion is appropriate. Energy levels are quantized, meaning there are specified energy distinctions where translational energies can physically "live." There is no continuous energy scale, as logic would suggest. As a result, relatively small fixed energy jumps are required to reach higher translational energy levels. Larger energy jumps are necessary to increase rotational levels, and successive gaps between these levels progressively increase as well. Vibrational energy jumps are the largest of the three, with successive vibrational energy level gaps decreasing in size [29]. Considering a diatomic molecule in translation, there are three associated thermal degrees-of-freedom. Each degree-of-freedom corresponds with a given $x - y - z$ coordinate direction. A rotat-

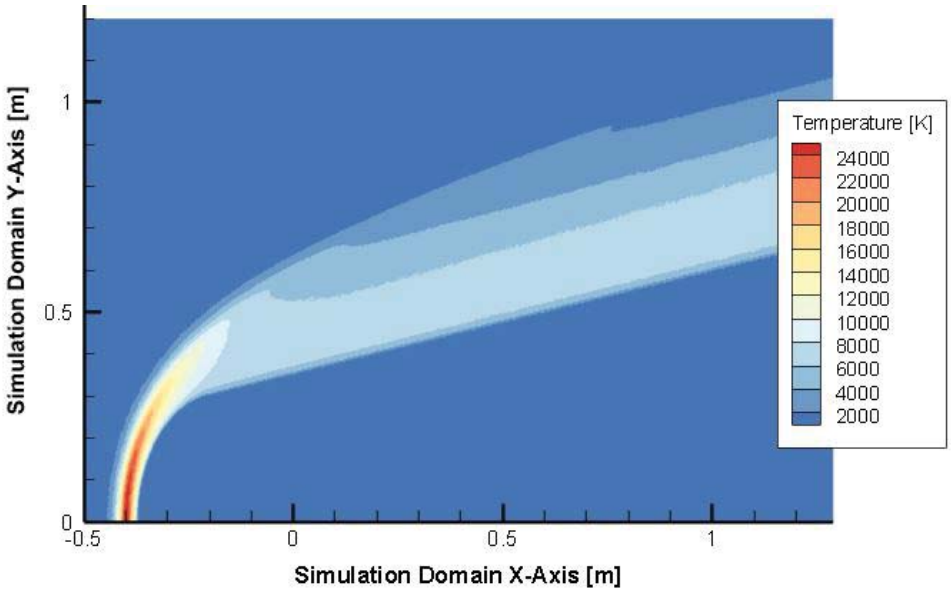

Figure 14. Translational Temperature Visualization (h=81 km)

ing diatomic molecule has two thermal degrees-of-freedom due to negligible rotation around the lengthwise bond, while a vibrating diatomic molecule has two thermal degrees of freedom, both from kinetic and potential vibrational motion [29].

The maximum stagnation temperatures for all profiles are seen in Table 3, with a total collision energy model[2] being used by all simulations. As expected, the maximum value is translational temperature at across all three simulations. Referring to Fig. 15, it is apparent that the translational maximum is reached further from the body than rotational and vibrational maximums. This is because translational energy modes are more easily excited than rotational and vibrational modes. The temperature trend has a gradual decline further into the freestream since it extends indefinitely. The steeper trends closer to the RAM C-II body is due to the short distance with which the temperature inside the shock decreases to the surface temperature of the vehicle.

[2]The total collision energy model, TCE, was published in Bird's *Molecular Gas Dynamics and the Direct Simulation of Gas Flows* in 1994, and is the most commonly used chemistry model in present-day DSMC simulations [9].

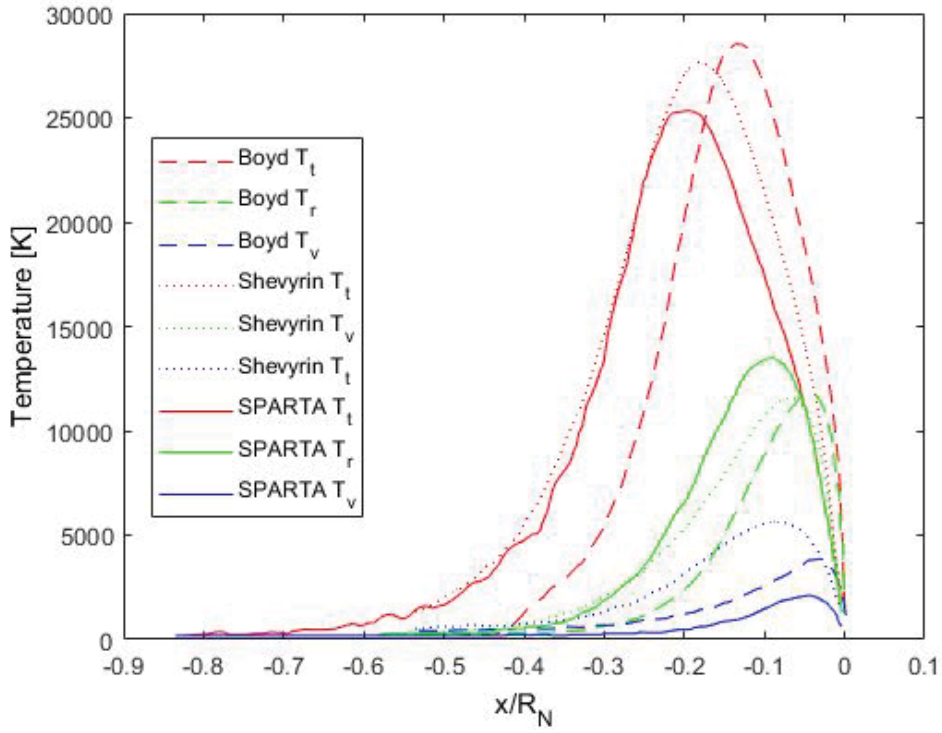

Figure 15. RAM C-II DSMC Stagnation Line Temperatures

Table 3 shows there are slight variations in the temperature values across the analyses. The programmed reactions, do however, vary slightly amongst each author's simulation, potentially affecting the temperatures. SPARTA's maximum translational temperature is 25300 K, over 2000 K less than Shevyrin's 27700 K and Boyd's 28500 K. Since recombination reactions are exothermic and are not currently supported by SPARTA with the ambipolar approximation, this is one feasible explanation for the

Table 3. DSMC Stagnation Line Temperature Comparisons

Maximum Temperatures [K]			
	T_t	T_r	T_v
SPARTA	25300	13500	2100
University of Michigan (Boyd)	28500	11800	3900
Novosibirsk University (Shevyrin)	27700	11600	5600

translational discrepancy [30]. SPARTA and Shevyrin translational profiles match very well up to $x/R_N = -0.225$, where Shevyrin's temperature continues to increase to 27700 K. Subsequently, the two profiles do converge to the vehicle's surface temperature of 1000 K; Boyd's simulation programmed a vehicle surface temperature of 1500 K, 500 K more than the SPARTA and Shevyrin simulations. It is worthwhile to note that Fig. 15's x/R_N distance of 0.1 is approximately 15/1000 of a meter. Each energy mode's maximum temperature locations amongst simulations are less than 15/1000 of a meter between one another. For example, the greatest distance between translational maximums is between SPARTA and Boyd simulations, at a distance of 11.3/1000 of a meter. Shevyrin and Boyd maximum rotational temperatures are nearly identical with only 200 K separating their rotational maximums, while SPARTA's maximum is about 1800 K higher than their average. Boyd's vibrational temperature of 3900 K almost lies directly in between SPARTA's 2100 K and Shevyrin's 5600 K. Shevyrin also ran simulations with two other chemistry models in addition to the TCE model, seen in the RAM C-II DSMC Stagnation Line Temperatures plot in [28]. The KSS (Kuznetsov-based state specific) and QK (quantum-kinetic) models illustrate the variation in simulation temperatures based on the chemistry model used.

SPARTA's translational value has an error of 10.0% as compared to averages of Boyd and Shevyrin analyses. In addition, SPARTA's rotational temperature contains 15.4% error as compared to the average of the other two analyses. The deviations in vibrational temperatures across all three analyses contain high error margins compared to the average of the other two analysis; SPARTA's is 55.8%, Shevyrin's is 86.7%, and Boyd's is 1.3%, with the latter falling in the middle of the other two temperatures. Overall, the temperatures profiles across all three DSMC simulations fall

within a reasonable range of one another with a mean error of 13.7%. Additionally, the mean error without vibrational temperature consideration is 5.4%.

3.3 Analytic Reentry Model

3.3.1 Assumptions and Limitations

There are a number of potential assumptions that can be considered when conducting reentry analysis. The first set that will be detailed are those associated with the reentry equations of motion. First, the spacecraft is assumed to be a constant point mass. The forces acting on the spacecraft are expressed by the following vector equation:

$$\vec{F} = \vec{T} + \vec{A} + m\vec{g} \tag{3.7}$$

where $\vec{T}$ is the thrust vector, $\vec{A}$ is the aerodynamic forces vector, m is the mass of the vehicle, and $\vec{g}$ is the gravitational force vector. Although $\vec{A}$ is comprised of both lift and drag forces, the latter is assumed to be the dominant force during reentry, and drag is assumed to act opposite velocity. This is a key component in using the kinematic equations to derive the force equations, and provides an orientation of the spacecraft reference frame and corresponding angles. Next, the lift vector is assumed perpendicular to the velocity vector. This angle relationship helps further define the spacecraft reference frame and enables the formulation of rate equations for the flight-path angle ($\dot{\gamma}$) and heading angle, ($\dot{\psi}$), both of which include lift and velocity terms [6]. The final assumption is that the force of gravity acts along the position vector $\vec{r}$ from the planetary center-of-mass to the spacecraft point mass. Based on this construct, the gravitational force is a function of the radius, as expressed by the following:

$$m\vec{g} = -mg\hat{e}_{x_2} \tag{3.8}$$

where the coordinate vector $\hat{e}_{x_2}$ is the x-component of the vehicle-pointing system reference frame, shown in Fig. 16 [6]. This coordinate system can be obtained through latitude ϕ and longitude θ coordinate transformations from the planet-fixed reference frame.

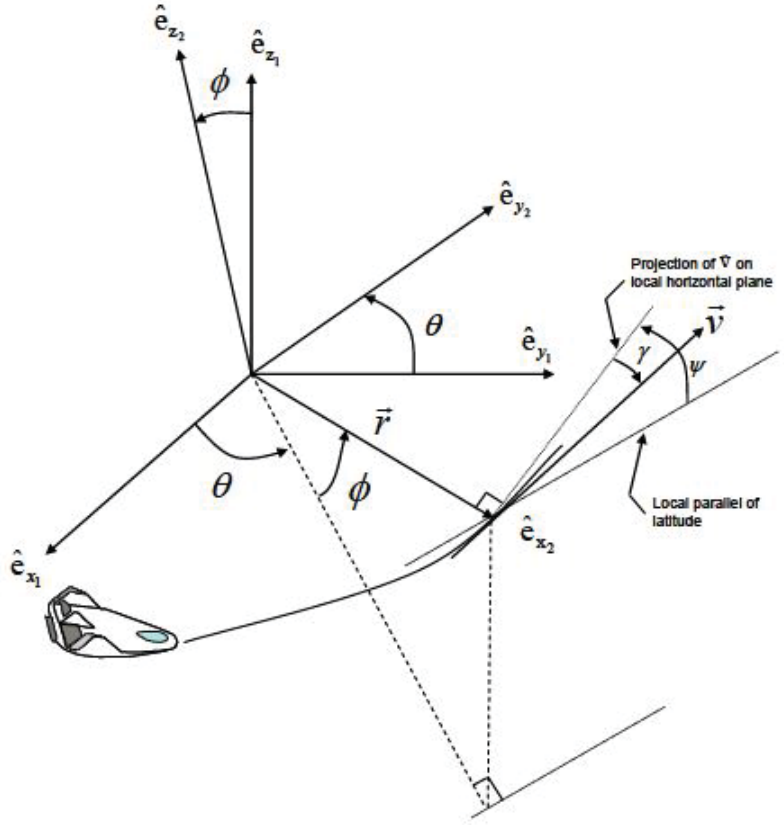

Figure 16. Vehicle Pointing System [6]

For all reentry simulations, an inertial geocentric equatorial reference frame is used and the Earth's rotation is ignored; rotation on the satellite's aerothermodynamic values are negligible given the limited time the satellite spends within the atmosphere. This could not be assumed if a specific landing location was targeted, but considering the objective is to determine aerothermodynamic values along the skip trajectory, it is valid for the analysis. The x-axis and z-axis point in the directions of the Vernal Equinox and the North Pole, respectively, while the y-axis is coplanar with the Earth's equatorial plane [6].

An important aspect of any reentry analysis is the atmospheric density model. For the present research, an exponential atmosphere model was selected as shown by the following:

$$\rho = \rho_s e^{-\beta(r-R_\oplus)} \tag{3.9}$$

where β is the inverse scale height, an assumed constant value of $\beta = 0.14$ km^{-1}; r is the distance from Earth's center of mass to the spacecraft; $R_\oplus$ is the radius of the Earth; and ρ_s is the density at sea level. The inverse square law of gravity model is also implemented, where g_s is the gravitational force at sea level, 9.81 m/s^2 [6].

$$g = g_s \left(\frac{R_\oplus}{r} \right)^2 \tag{3.10}$$

3.3.2 Equations of Motion

For the present research, the aerothermodynamic properties of various skip entry trajectories will be evaluated for the given satellite body. During skip entry, the most stressing conditions are at perigee, where the satellite will experience the highest aerothermodynamic loading of the trajectory. In order to conduct analysis with SPARTA, the speed corresponding to various perigee locations of select skip trajectories is required. To find these perigee speeds, an analytic skip entry analysis will be executed using the equations of motion given by Eqs. (3.11)-(3.16). The kinematic equations of motion are time derivatives of position r, longitude θ, and latitude ϕ, while the force equations are time derivatives of velocity V, flight-path angle γ, and

heading angle ψ.

$$\dot{r} = Vsin\gamma \tag{3.11}$$

$$\dot{\theta} = \frac{Vcos\gamma cos\psi}{rcos\phi} \tag{3.12}$$

$$\dot{\phi} = \frac{Vcos\gamma sin\psi}{r} \tag{3.13}$$

$$\dot{V} = -\frac{D}{m} - gsin\gamma + r\omega_{\oplus}^2 cos\phi\left(cos\phi sin\gamma - sin\phi sin\psi cos\gamma\right) \tag{3.14}$$

$$\begin{aligned}\dot{\gamma} = \Bigg(&\frac{L}{m}cos\sigma - gcos\gamma + \frac{V^2}{r}cos\gamma \\ &+ 2V\omega_{\oplus}cos\phi cos\psi + r\omega_{\oplus}^2 cos\phi\left(cos\phi cos\gamma + sin\phi sin\psi sin\gamma\right)\Bigg)/V\end{aligned} \tag{3.15}$$

$$\begin{aligned}\dot{\psi} = \Bigg(&\frac{1}{mcos\gamma}\left(Lsin\sigma\right) - \frac{V^2}{r}cos\gamma cos\psi tan\phi \\ &+ 2V\omega_{\oplus}^2\left(sin\psi cos\phi tan\gamma - sin\phi\right) - \frac{r\omega_{\oplus}^2}{cos\gamma}sin\phi cos\phi cos\psi\Bigg)/V\end{aligned} \tag{3.16}$$

The six equations of motion include drag and lift terms, given by Eqs. (3.17) and (3.18), where C_D and C_L are the vehicle drag and lift coefficients, respectively, and S is the vehicle reference area. The equations for the density ρ and the gravitational constant g are rewritten here for completeness, as they are also variables within the reentry equations of motion. Table 4 includes the parameter values used in the previous reentry equations as well.

$$D = \frac{\rho C_D S}{2}V^2 \tag{3.17}$$

$$L = \frac{\rho C_L S}{2}V^2 \tag{3.18}$$

$$\rho = \rho_s e^{-\beta(r-R_{\oplus})} \tag{3.9}$$

$$g = g_s\left(\frac{R_{\oplus}}{r}\right)^2 \tag{3.10}$$

Table 4. Parameter Values within the Equations of Motion

Parameter	Value
C_D	2.2
C_L	0.4
ρ_S	1.225 kg/m^3
g_S	9.81 m/s^2
$R_\oplus$	6378.137 km
β	.14 km^{-1}

The force equations of motion are partially derived based on the assumption that drag force acts opposite velocity, and drag can be expressed in the velocity-referenced frame as follows:

$$\vec{D} = -D\hat{e''_y} = -D\hat{e_v} \tag{3.19}$$

The second term in Eq. (3.19), $-D\hat{e''_y}$, is the magnitude of drag along the y''-axis of the "Flight-Path Angle Rotation" coordinate system in Fig. 17. To understand the orientation of this velocity-referenced frame, the vehicle-pointing system in Fig. 16 is revisited. A rotation of the heading angle ψ is required around the x_2-axis until the velocity vector's horizontal plane projection matches the $\hat{e}'_y$-axis. This is illustrated nicely by the "Heading Angle Rotation" coordinate system in Fig. 17. Subsequently, a rotation of γ around the z'_2-axis aligns the velocity vector with the $\hat{e}''_y$-axis, with the $\hat{e}''_z$-axis pointing out of the page [6]. Equation (3.19) can be further divided into components of the drag forces using γ and ψ rotation angles:

$$\vec{D} = -(Dsin\gamma\hat{e}_{x2}) - (Dcos\gamma cos\psi\hat{e}_{y2}) - (Dcos\gamma\ sin\psi\hat{e}_{z2}) \tag{3.20}$$

The three-dimensional reentry model can be reduced into the two-dimensional pla-

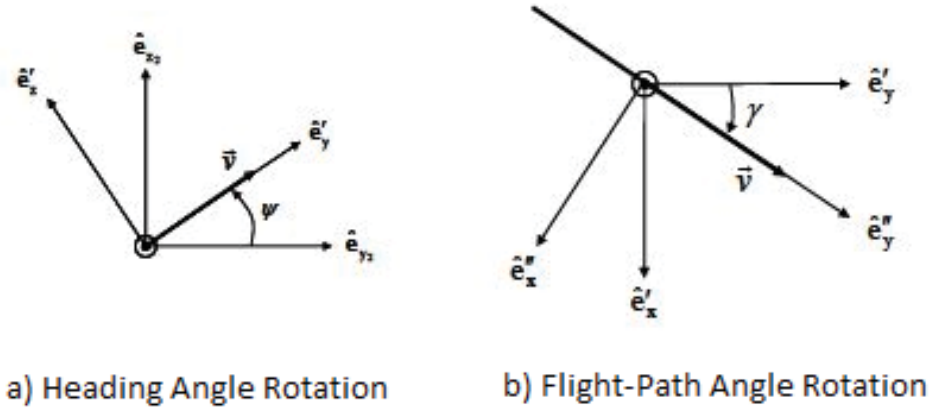

Figure 17. Coordinate Transformation: Vehicle-Pointing to Velocity-Referenced [6]

nar model shown in Fig. 18. In this figure, the lift vector is perpendicular to the spacecraft's velocity vector, and the flight-path angle is the angular distance from the local horizontal plane to the velocity vector. In order to maintain planar entry, the bank is assumed to be negligible. In addition, ignoring Earth's rotation reduces the force equations of motion to the following:

$$\dot{V} = -\frac{D}{m} - gsin\gamma \tag{3.21}$$

$$\dot{\gamma} = \left(\frac{L}{m} - gcos\gamma + \frac{V^2}{r}cos\gamma\right)/V \tag{3.22}$$

$$\dot{\psi} = \left(-\frac{V^2}{r}cos\gamma cos\psi tan\phi\right)/V \tag{3.23}$$

A determination of the aerothermodynamic parameters at skip perigee does not require knowledge of the spacecraft's position with respect to Earth. Therefore, only solutions to the position, velocity, and flight-path angle equations of motion are necessary, while latitude, longitude, and heading angle values are unnecessary. The planar entry equations can be reduced from six to three, with the final equations of motion

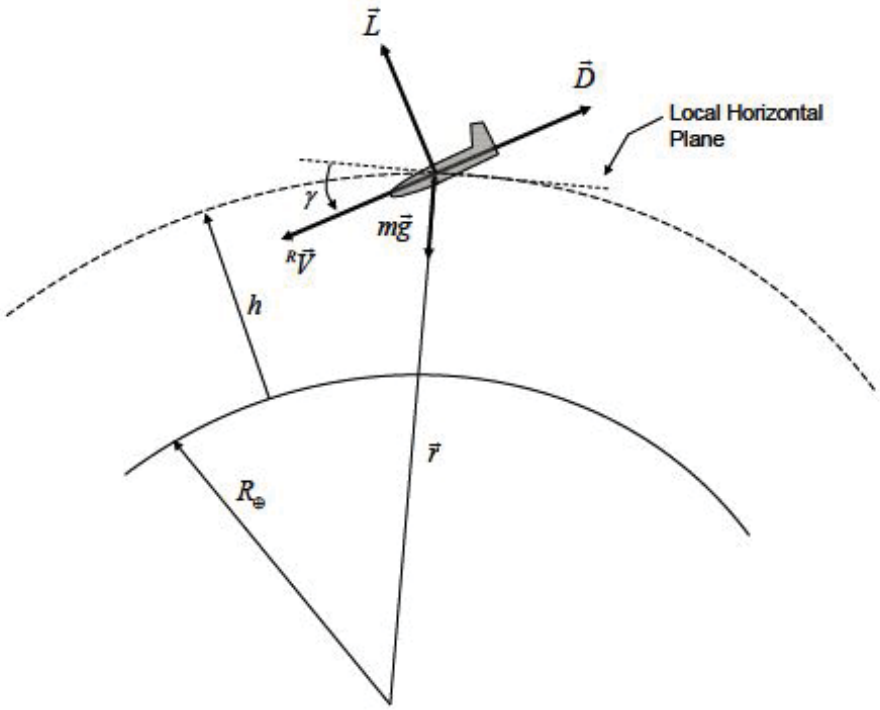

Figure 18. 2D Planar Entry [6]

written below:

$$\dot{r} = V sin\gamma \tag{3.11}$$

$$\dot{V} = -\frac{D}{m} - gsin\gamma \tag{3.21}$$

$$\dot{\gamma} = \left(\frac{L}{m}cos\sigma - gcos\gamma + \frac{V^2}{r}cos\gamma\right)/V \tag{3.22}$$

These equations are limited to numerical analysis, but the non-dimensional form can be obtained and solved analytically. Equations (3.24)-(3.26) include these substitutions, with T representing the non-dimensional altitude comprised of g_0, the gravitational constant at sea level, and r_0 the reference radial distance to the spacecraft.

$$T = \frac{1}{2}\frac{V^2}{g_0 r_0} \tag{3.24}$$

$$\xi = cos\gamma \tag{3.25}$$

$$\eta = \frac{\rho S C_D}{2m\beta} \tag{3.26}$$

Equation 3.25 for ξ is a variable substitution for flight-path angle, and η is the non-dimensional altitude. Through a series of substitutions, simple derivations, and an exponential atmospheric assumption, the dimensional equations of motion are converted to non-dimensional terms as given by Eqs. (3.27) and (3.28).

$$\frac{dT}{d\eta} = \frac{2T}{sin\gamma} + \frac{1}{\beta r_0 \eta} \tag{3.27}$$

$$\frac{d\xi}{d\eta} = \frac{C_L}{C_D} + \frac{1}{\beta r_0 \eta}\left(1 - \frac{1}{2T}\right)\xi \tag{3.28}$$

Assuming the lift-to-drag ratio remains constant and the force of gravity is dominated by aerodynamic forces, the non-dimensional equations further reduce to:

$$\frac{dT}{d\eta} = \frac{2T}{sin\gamma} \tag{3.29}$$

$$\frac{d\xi}{d\eta} = \frac{C_L}{C_D} \tag{3.30}$$

which represent the non-dimensional equations for planar skip entry. Using these equations, the perigee velocities and altitudes can be obtained. First, the non-dimensional altitude is given by Eq. (3.31):

$$\eta = \frac{\rho S C_D}{2m\beta} e^{-\beta h} \tag{3.31}$$

$$\eta = \eta_e + \frac{cos\gamma - cos\gamma_e}{\left(\frac{C_L}{C_D}\right)} \tag{3.32}$$

With the non-dimensional altitude at perigee η known, the corresponding entry flight-path angle at 120 km is found by solving for γ_e in Eq. (3.32). The 120 km entry interface is the altitude above Earth's surface where the spacecraft re-enters the atmosphere, which is related to the entry radius r_0 = 6498.137 km, the sum of that altitude plus the radius of the Earth equivalent to an average value of 6378.137 km. After determining γ_e, it is known the flight-path angle at perigee γ_p is equal to zero, because the spacecraft's velocity vector $\vec{V}$ will be perpendicular to the position vector $\vec{r}$, seen more clearly in Fig.18. With the flight-path angle defined as the angle between the spacecraft's velocity vector and the local horizontal plane, then the spacecraft's velocity vector will transition from a negative to positive quantity at perigee where γ=0°.

The velocity at perigee V is subsequently solved using Eq. (3.33), with a known entry flight-path angle γ_e from Eq. (3.32). However, the entry velocity V_e is still unknown.

$$\frac{V}{V_e} = exp\left[\frac{-(\gamma - \gamma_e)}{(C_L/C_D)}\right] \tag{3.33}$$

To obtain V_e, Hohmann transfer equations can be utilized with an initial orbiting altitude and a target entry altitude of 120 km. The semi-major axis a_t can be found using

$$a_t = \frac{r_i + r_p}{2} \tag{3.34}$$

with r_i being the initial orbit radius and r_p being the perigee radius. The specific mechanical energy of the transfer ellipse can be found using

$$\epsilon_t = -\frac{\mu}{2a_t} \tag{3.35}$$

where Earth's gravitational parameter $\mu = 398600.44$ km^3/s^2 [31]. With the specific mechanical energy known, the velocity at the entry interface can be found from

$$V_e = \sqrt{2\left(\frac{\mu}{r_e} + \epsilon_t\right)} \tag{3.36}$$

Consequently, the only unknown variable in Eq. (3.33) is the velocity at perigee V, which can be found for varying entry altitudes and flight-path angles. The satellite's skip perigee velocities are given in Table 5, corresponding to perigee altitudes $h_p \in [90, 120]$ km. For all cases, the satellite is in a 400-km altitude circular orbit prior to executing a Hohmann transfer to the 120-km entry interface. It is important to note that the initial orbital altitude should significantly affect the aerothermodynamic DSMC computational output parameters; the orbital altitude alters the skip perigee velocities, ultimately changing the kinetic energy of the entry spacecraft. The mini-

Table 5. Entry Interface to Skip Perigee Parameters: X, Z-Directed Flow Orientations

Entry Interface [h_e = 120 km]		Perigee	
Flight-Path Angle γ_e	Velocity V_e [km/s]	Altitude h_p [km]	Velocity V_p [km/s]
0.00°	7.914	120	7.914
-0.09°	7.911	110	7.841
-0.21°	7.909	100	7.751
-0.43°	7.906	90	7.584

mum perigee altitude is restricted to 90 km, because typical satellite configurations will begin to experience destructive aerothermodynamic effects below this constraint, compromising structural integrity from aerodynamic forces and thermal heating. In addition, the satellite velocity will decrease at lower altitudes, thus reducing energy for subsequent maneuvers upon skip completion.

It is important to note that the analysis for the y-directed flow failed to account for the increased surface area of 2.59 m^2 with the inclusion of the solar panels, versus the .49 m^2 that was used for all orientations. Neglecting the solar panel surface area for the x-directed and z-directed flows, though not ideal, is closer to the correct solution than for the y-directed flow, as the thin depth of the solar panel is initially exposed to the incoming flow for those two scenarios. Overall, the use of .49 m^2 for the y-directed flow versus the more accurate 2.49 m^2 affects the perigee velocities based on the surface area value being embedded in the skip entry and Hohmann transfer equations of motion. The solar panels surface areas, thought, were not completey ignored for the y-directed flow, based on satellite simulation geometry solar panels still being exposed to the incoming flow of particles. Further analytic analysis, including solving the reentry and Hohmann transfer equations of motion with the 2.49 m^2 surface area, reveals the y-directed flow perigee velocities, shown in Table 6. A decrease to

Table 6. Entry Interface to Skip Perigee Parameters: Y-Directed Flow Orientation

Entry Interface [h_e = 120 km]		Perigee	
Flight-Path Angle γ_e	Velocity V_e [km/s]	Altitude h_p [km]	Velocity V_p [km/s]
0.00°	7.914	120	7.914
-0.21°	7.911	110	7.750
-0.48°	7.909	100	7.551
-0.99°	7.906	90	7.186

7.186 km/s in the minimum perigee velocity is apparent, as well as an increase in the entry interface flight-path angle up to a magnitude of .99°. Further SPARTA DSMC computational analysis is necessary to determine the aerothermodynamic variables upon accounting for the solar panel surface area for the y-directed flow.

3.4 Summary

This chapter discussed the DSMC simulator SPARTA, the skip entry analytic solution to the reentry equations of motion, and the assumptions and limiting factors related to these analytic solutions. These assumptions include the use of an exponential atmosphere, a spherical gravity potential, and an inertial geocentric equatorial coordinate system. Further, reentry bank angle and thrust force are neglected to reduce the preliminary three degree-of-freedom model. Experimental and simulated RAM C-II electron densities and stagnation temperatures were compared to evaluate SPARTA's computational accuracy. Though the computed electron densities were higher than the experimental data, this is likely attributed to the lack of support for recombination reactions when fix ambipolar is implemented. Despite this difference in density, the temperature contours and stagnation streamline profiles from the validation study match adequately well with the other DSMC analyses [24, 28]. Fair confidence in SPARTA's simulation capabilities for high-altitude flow encountered during reentry can be established based on the analysis contained in this chapter. Finally, various perigee speeds were determined from the skip reentry equations of motion for use with DSMC analysis for a generic satellite at skip perigee.

IV. Analysis and Results

4.1 Chapter Overview

This chapter will examine the satellite aerothermodynamic effects on skip pergiee altitudes $h_p \in [90, 120]$ km; specifically, the maximum surface pressure, surface force, temperature, and heat flux effects. In addition, the computational heat flux will be compared to closed-form equations, and a determination of a practical perigee limit for the skip trajectory is realized.

4.2 DSMC Results

Three flow orientations were selected for each altitude in order to compare the aerothermodynamic effects with varying exposed surface configurations, shown in Figs. 19, 20, and 21. In Fig. 19, the incoming flow is traveling in the positive x-direction, colliding with the shorter solar panel edge first, followed by the 0.49 m^2 surface area of the main satellite body. In Fig. 20, the positive y-oriented flow contacts the satellite from below, engaging a greater exposed surface area than the other two configurations. Though the flow in these three figures is visualized as a two-dimensional slice, the simulation domain is a cubic area. Finally, flow traveling in the positive z-direction is shown by Fig. 21, with initial collisions impacting the solar panel thickness, lengthwise, and the 0.49 m^2 area perpendicular to the flow.

Table 7 shows the functions used to fit the pressure P, force F, heat flux $\dot{q}$, and temperature T data points corresponding to each perigee altitude. Each parameter was measured at three orientations, with "X" representing flow traversing the positive x-direction, and "Y" and "Z" following the same convention for each satellite orientation, regression curves can be fit to the aerothermodynamic properties computed by SPARTA at each of the analyzed skip perigee altitudes. All pressure and force

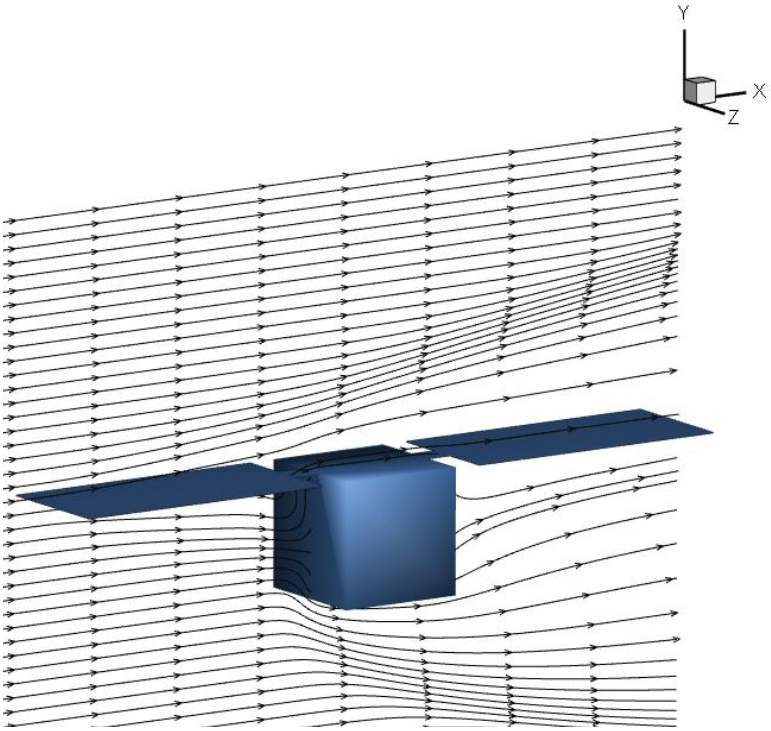

Figure 19. Simulation Flow: Positive X-Direction

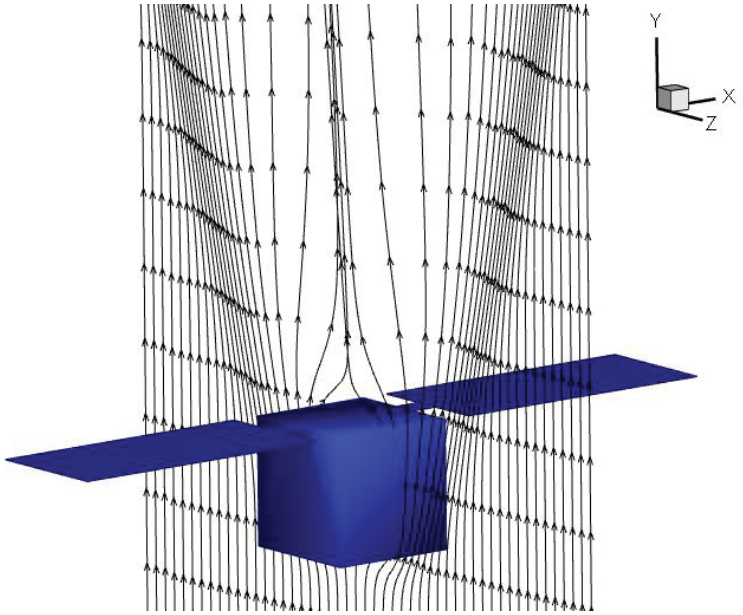

Figure 20. Simulation Flow: Positive Y-Direction

data fits are power functions in form, while the heat flux and temperature functions are second-and third-order polynomials, respectively. The regression functions do

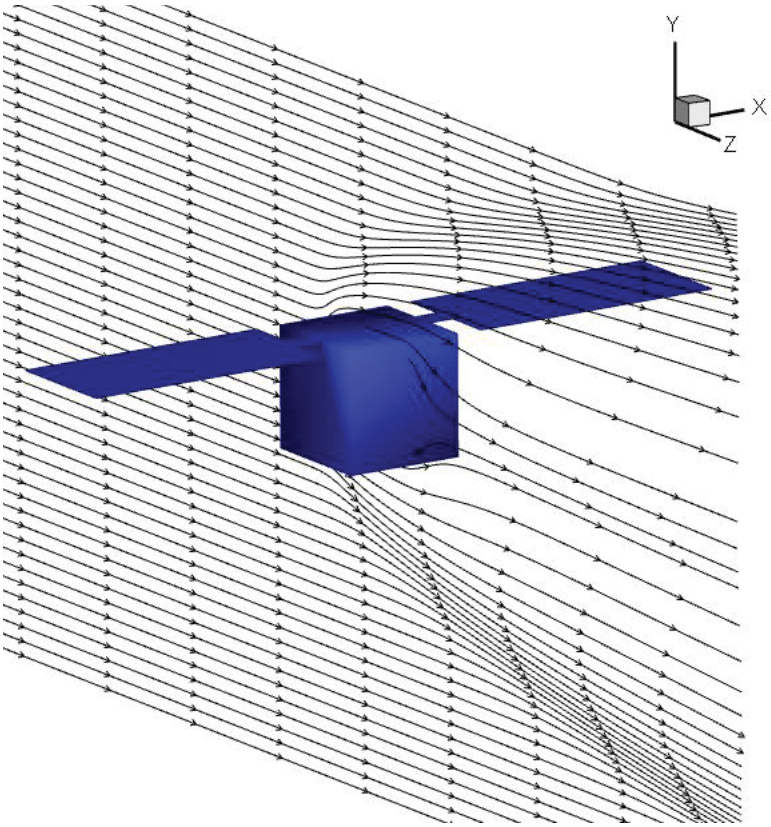

Figure 21. Simulation Flow: Positive Z-Direction

not necessarily match the data exactly, but rather attempt to approximate the values based on the exact computational data markers shown in the upcoming plots. These data markers correspond with the four equidistant perigee altitudes from 90 km to 120 km. The coefficient of determination (R^2) values, also given Table 7, vary from approximately 0.91 to 1.00 of the regression curves formulated, one quarter feature $R^2 = 1.00$ which indicates a perfect fit for the given data points.

Figure 24 shows the computational results of the surface pressures exerted on the satellite. A typical satellite configuration experiences the most stressing conditions at a skip perigee of 90 km, approximately the lowest survivable altitude it can withstand during reentry prior to experiencing irrecoverably destructive aerothermodynamic effects. Based on the pressure profiles, it is evident that the z-oriented flow produces

Table 7. Parameter Data Point Curve Fits

Parameter	Orientation	Fit	R^2
P	X	$P=(3 \times 10^{36})h^{-17.59}$	0.9974
	Y	$P=(2 \times 10^{34})h^{-16.56}$	0.9980
	Z	$P=(1.8 \times 10^{37})h^{-17.94}$	1.0000
F	X	$P=(4 \times 10^{32})h^{-16.10}$	0.9984
	Y	$P=(7 \times 10^{32})h^{-16.01}$	0.9976
	Z	$P=(1 \times 10^{33})h^{-16.21}$	0.9989
$\dot{q}$	X	$P=-24.6h^2+3467.9h-59846$	0.9166
	Y	$P=-15.1h^2+1445.9h+46233$	0.9354
	Z	$P=-13.0h^2+1030.0h+66800$	0.9427
T	X	$P=0.78h^3 - 255.5h^2 + 27747h - 976900$	1.0000
	Y	$P=0.53h^3 - 174.3h^2 + 19051h - 667530$	1.0000
	Z	$P=0.74h^3 - 240.3h^2 + 25971h - 908920$	1.0000

the highest surface pressures on the satellite, followed by the x-oriented and z-oriented flows.

In Fig. 22, the location of maximum pressure at a 90 km skip perigee occurs at the right corner of the solar panel, where it experiences the greatest exerted pressure force of 155.8 Pa. As the incoming flow collides with the satellite body, a coupled moment is applied to the thin solar panel. If the solar panel was infinitely long, then a more consistent pressure distribution would be applied over the 1.5-m distance the flow traverses. The second largest observed pressure value is 125.1 Pa, which is at the top left surface of the same solar panel, but not visible in Fig. 22. The pressure values over the cubic satellite body's exposed surface are $P \in [50, 90]$ Pa. The majority of these values are $P \in [80, 100]$ Pa, concentrated within the center 0.25 m^2 of the total 0.49 m^2 surface area. The lower surface of the solar panel's actuator arm experiences average pressures of 100 Pa along the inner

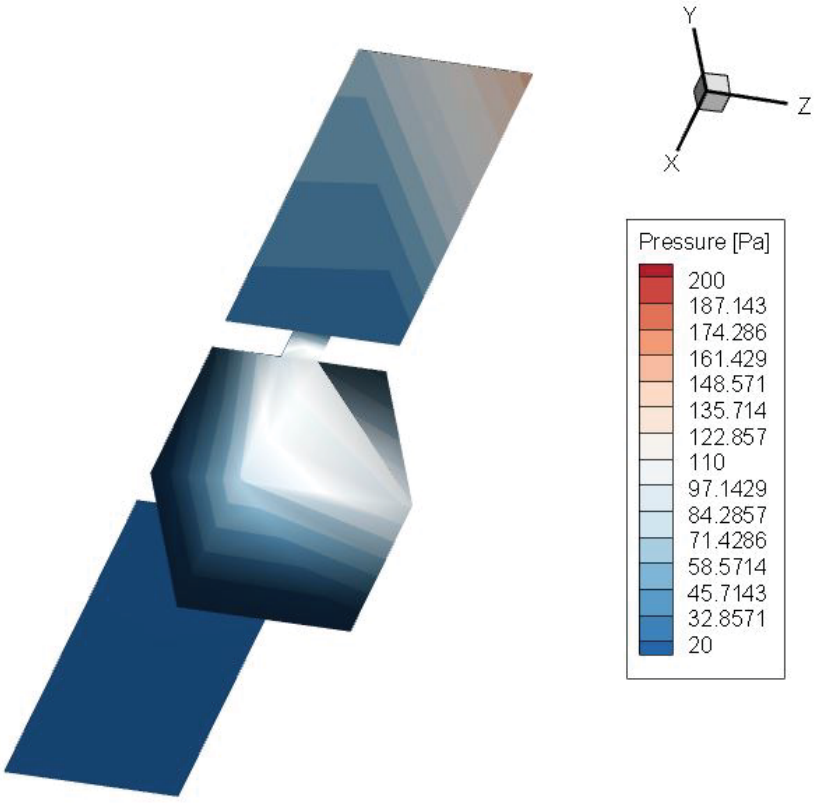

Figure 22. Pressure Distribution: 90 km, Flow Positive X-Direction

third, adjacent to the main body. The average pressure drops to 62 Pa at the outer two-thirds of the actuator adjacent to the solar panel. The base of the actuator is a likely failure point for material fracture as a result of the total force applied to the solar panel from the vertical flow.

Figure 23 shows the maximum y-directed flow pressures. In this orientation, moments are exerted at each solar panel, thereby causing an increase in the actuator's pressure per unit area. The final orientation is shown in Fig. 25 with the z-oriented pressure distribution. The maximum value occurs once again at a panel's surface corner, indicated by the red distribution where P = 174.6 Pa. It should be clarified that this pressure occurs on the top surface of that corner, not along its edge. Nevertheless, the pressure distribution along the edge is upwards of 100 Pa. The second greatest

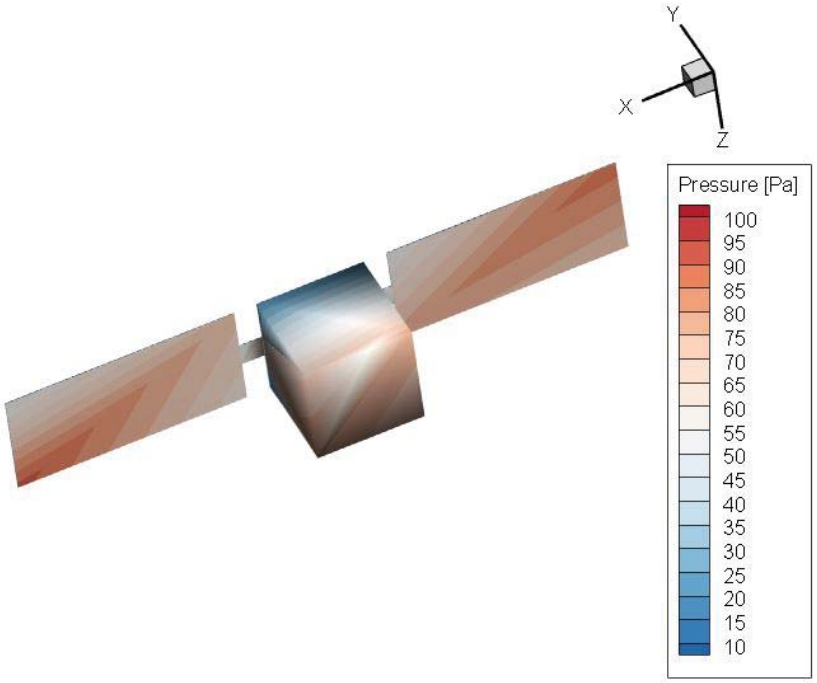

Figure 23. Pressure Distribution: 90 km, Flow Positive Y-Direction

pressure, 128 Pa, is exerted on the leading edge of the same solar panel, at the bottom end of its extended side. The left solar panel should experience similar values at its respective symmetric corners. However, pressures exerted on the right solar panel are greater than the left, because the satellite was located at the far side of the simulation domain. The left solar panel's tip is adjacent to the simulation domain face, with the overall satellite centered from top to bottom. Specular reflection was programmed for particles colliding with that face, generating a greater number of particles travelling diagonally into the body. Despite the apparent color transition across the satellite's main body, pressures are uniformly distributed across the satellite's main body face.

The surface pressure profiles for all altitudes are power functions, shown in Fig. 24. SPARTA's computational output data values are specified by the various markers in the figure. The profiles indicates the pressure increases dramatically from 100 km to 90 km, an average of 7.4 times greater over each orientation. This shows that the

number density of the ambient air greatly affects pressure quantities on re-entering vehicles. Satellite re-entries descending to altitudes below 90 km will experience detrimental stresses affecting structural integrity, supporting the research that typical satellite configurations will breakup between h ∈ [75, 85] km [32]. At 120 km, the computational data indicates pressure values for all orientations are within .2 Pa of one another; the pressure values for x, y, and z orientations are 1.0 Pa, 0.8 Pa, and 1.0 Pa, respectively. The pressure quantities at this altitude are minimal due to a two order of magnitude decrease in number density. This results in fewer molecule collisions with the satellite, thus making the pressure difference between orientations negligible when the exerted force is insubstantial.

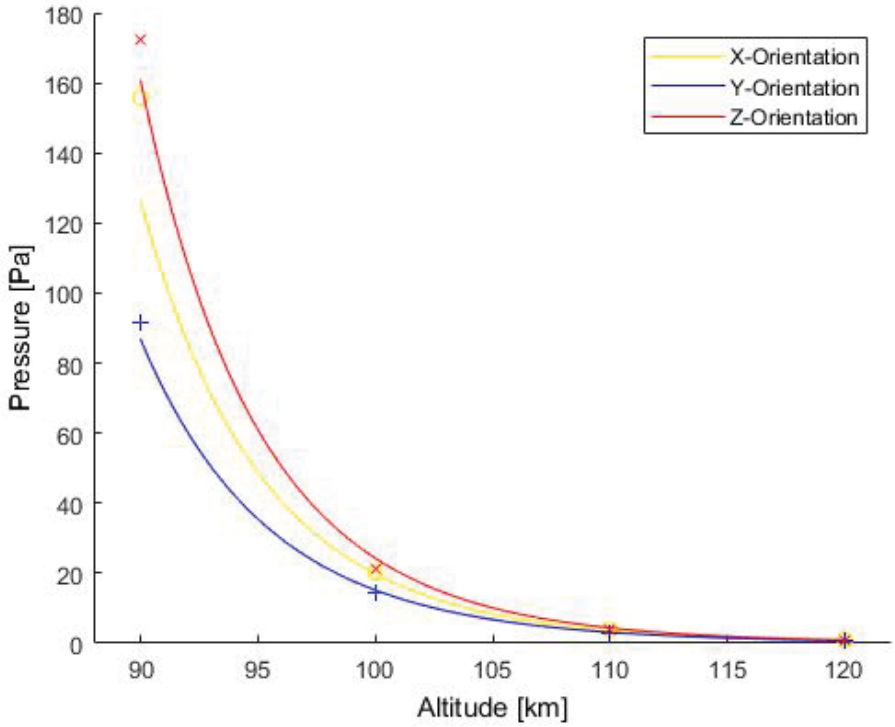

Figure 24. Maximum SPARTA Skip Perigee Surface Pressure

It is important to note that the grid used in these satellite simulations does not currently accurately capture *all* particle collisions. The grid coded was (100 x 100 x 100), while the mean free path indicates that a (166 x 166 x 166) grid is necessary for the

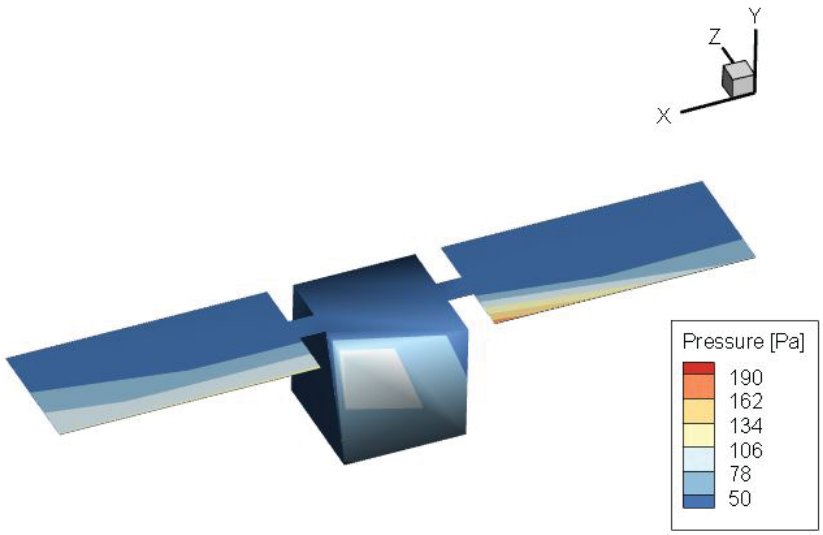

Figure 25. Pressure Distribution: 90 km, Flow Positive Z-Direction

freestream region of the most dense 90 km altitude. The timestep was also coded as 3.47 x 10^{-6}, while the mean collision time was calculated to be 5.78 x 10^{-7}. The timestep should be less than the mean collision time in order to accurately capture all collisions. However, a 6.00 x 10^{-7} timestep is necessary to capture the most frequent collisions in the most dense regions of the flow the larger the timestep used in the present analysis does not mean the (100 x 100 x 100) grid computations are entirely incorrect; instead, the computations are approximations that will inevitably contain a percent error. Table 8 shows the necessary grid refinement for freestream flow at corresponding perigee altitudes. All freestream grid sizes are more refined than necessary except for 90 km, at which point a (200 x 200 x 200) grid simulation was executed. Though the simulation and subsequent post-processing was a success, a lack of computer memory upon file transfer led to the presentation of the (100 x 100 x 100) grid results. To capture all collision regions, including the most dense near the satellite body, a grid greater than (166 x 166 x 166) would be necessary. An analytic solution to the surface pressure values at 100 km was calculated as well, and

Table 8. Ambient Grid Size

Altitude [km]	Grid Size
90	(166 x 166 x 166)
100	(25 x 25 x 25)
110	(4.7 x 4.7 x 4.7)
120	(1.1 x 1.1 x 1.1)

the computational output is within 2 Pa of the analytic solution. Available memory restricted the initial grid refinement, but further analysis will likely lead to more accurate aerothermodynamic values.

The surface forces on the satellite were analyzed as well. The force trendlines should appear similar to the pressure profiles considering the two variables are functions of one another. Upon examining Fig. 26, it is apparent that the plots do have similar trends. The force-pressure relation is shown below:

$$F = PA \tag{4.1}$$

From this equation, it is easily understood that the y-oriented flow produces the greatest force on the satellite, considering it has largest exposed surface area at 1.54 m^2. Further, the z-oriented flow contacts a surface area of 0.49 m^2, while the x-oriented flow encounters a 0.54 m^2 face. These areas include the thickness of the .07 m solar panels as well. At the entry interface, where h_e = 120 km, the forces for all orientations are within 0.26 N of each other. The force exerted on the y-oriented satellite is shown in Fig. 27 for comparison with the pressure distribution in Fig. 23. The maximum moment is based on the following equation:

$$M = Fd \tag{4.2}$$

where d is the distance to the point or axis of rotation. When calculating the maximum moment, a 38.9 N force is multiplied by the .35 m distance to x-axis of rotation; a 13.6 N-m moment is generated. The similar y-oriented pressure and force figure distributions confirm the force-pressure relationship in Eq. (4.1). In addition, the maximums occur in the same location, which is on the underside of the solar panels' corner surfaces.

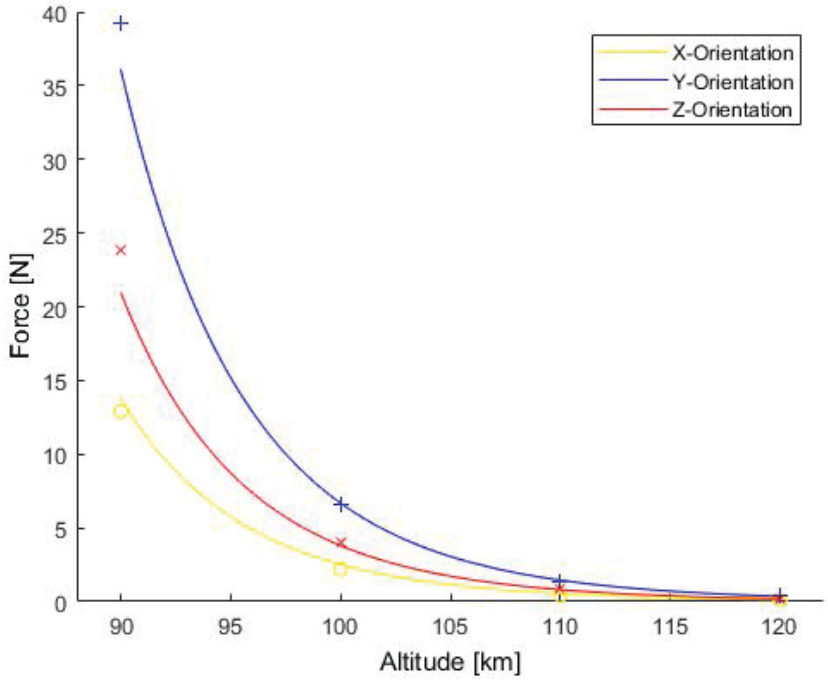

Figure 26. Maximum SPARTA Skip Perigee Surface Force

The computational flow field temperature data is shown by the markers in Fig. 28, with a cubic polynomial fit of each regression function. As shown in this figure, the regression functions decrease from 120 km to 90 km, which is ultimately due to the decrease in velocity. This results in a decrease in the temperature based on the exponential dependence of temperature on velocity. The values are also in the correct range for a reentry vehicle, with the satellite's $T \in [21500, 27370]$ K across all simulations. All exact computational temperatures, indicated by the markers, are monotonically increasing from 90 km to 120 km.

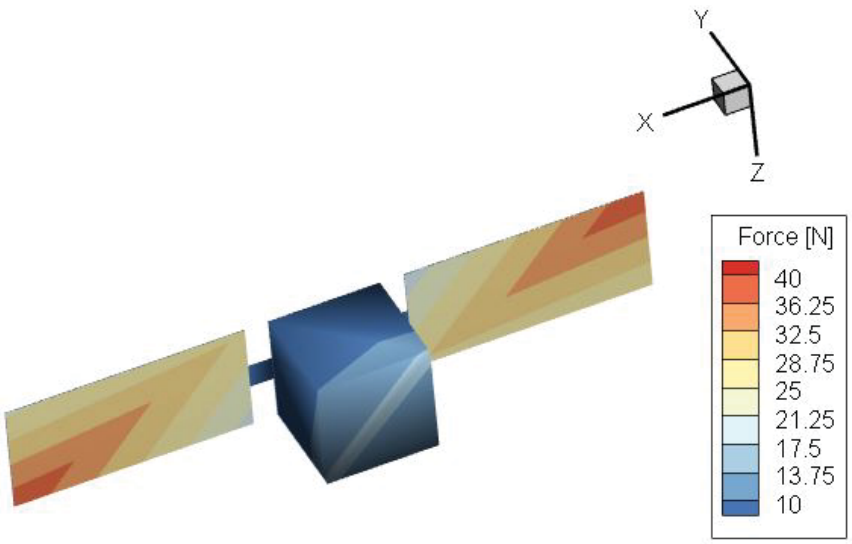

Figure 27. Force Distribution: 90 km, Flow Positive Y-Direction

Figure 29 illustrates the grid temperatures for the y-directed flow. The satellite is adjacent to the left side of the simulation domain, which is not an ideal position for flow analysis. A potential change for future simulations is to center the satellite body based on flow direction to improve the clarity of data output. As the hypersonic freestream flow encounters the satellite body, numerous shock interactions are apparent. A detached shock forms over the main satellite body, which quickly impinges on another shock generated around the solar panel. This shock-shock interaction complicates the flow field, with a mix of hypersonic, supersonic, and subsonic flow regions present. Chemical reactions occur within these shocks, considering the activation energies of most reactions are exceeded, including some ionization reactions, based on the kinetic energy of the impending flow. Pressures and temperatures increase across the shock as the velocity of the flow dramatically decelerates. The expansion region beyond the outer edge of the solar panel results in an increase in velocity and a decrease in pressure, temperature, and density [29, 33].

Finally, the heat flux computational values are examined for the satellite at skip perigee, with a second order polynomial used to fit the data for all altitude cases.

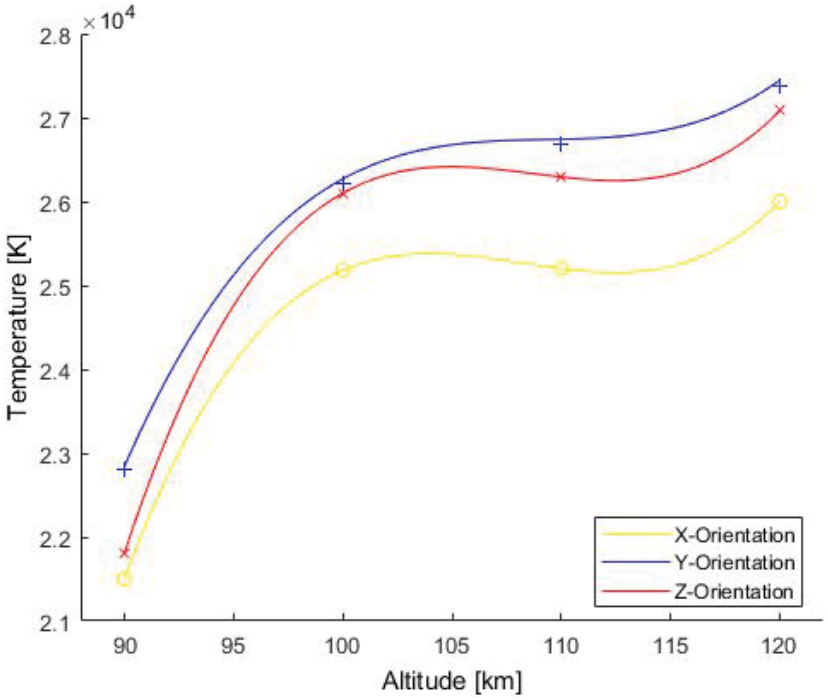

Figure 28. Maximum SPARTA Skip Perigee Temperature

The 120-km average heat flux value across the three orientations is 5286 kW/m^2, with an average error of 0.2%. The heat fluxes at 110 km increase by approximately 150%, with an additional 300% at 100 km. Values at this perigee altitude range from $\dot{q}$ = [46700, 49100] kW/m^2. Fig. 31 shows the heat flux grid profile at 110 km for x-oriented flow. The flow appears to be affected by updraft flow originating from collisions with the satellite body, where a region of high heat flux values is observed close to the center of the surface face. The values decrease by approximately 300 kW/m^2 as the flow approaches the lateral edge of that face, along its centerline. Overall, the computational heat flux values are significantly higher than expected. One could conclude, strictly based on the data, that 120 km is not a survivable altitude for a satellite reentry descent. However, according to Tewari, the maximum heat flux for a reentry *capsule* prior to breakup is only 1800 kW/m^2 [34]. Because a satellite is not typically built with survivable re-entry in consideration, breakup would occur well below the 1800 kW/m^2 heat flux threshold. It should be noted that

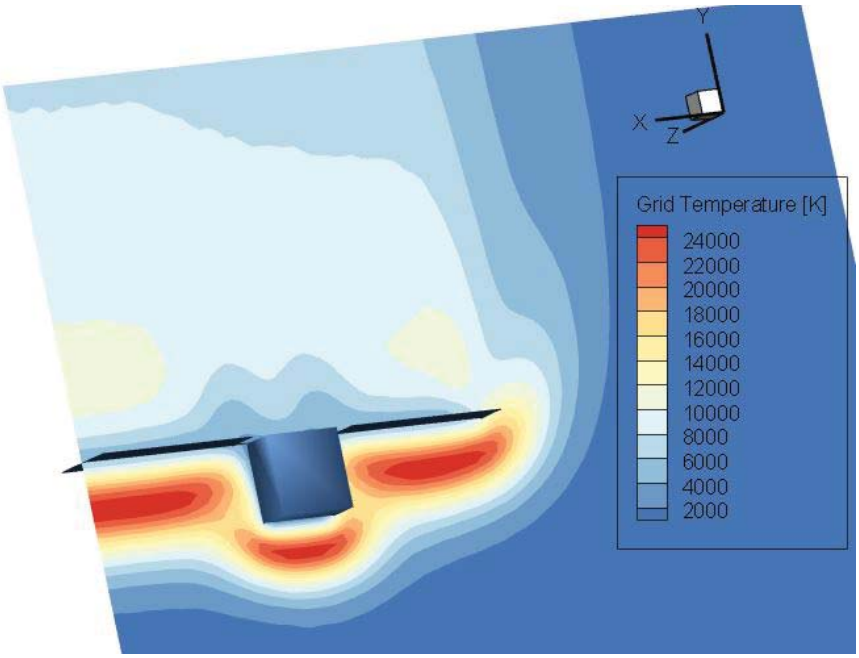

Figure 29. Grid Temperature: 100 km, Flow Positive Y-Direction

SPARTA does output multiple heat flux values depending on the group of species associated with the mixture. The group that produced the high heat flux values plotted in Fig. 30 was associated with neutral species only. The group containing electrons e^- and ions NO^+ produced approximate heat flux values ranging from $\dot{q} \in$ [.00, 360] kW/m^2. These values are more feasible reentry heat fluxes for a satellite skip entry trajectory at perigee, and are tabulated in the next section for comparison with the recorded heat flux values in this section.

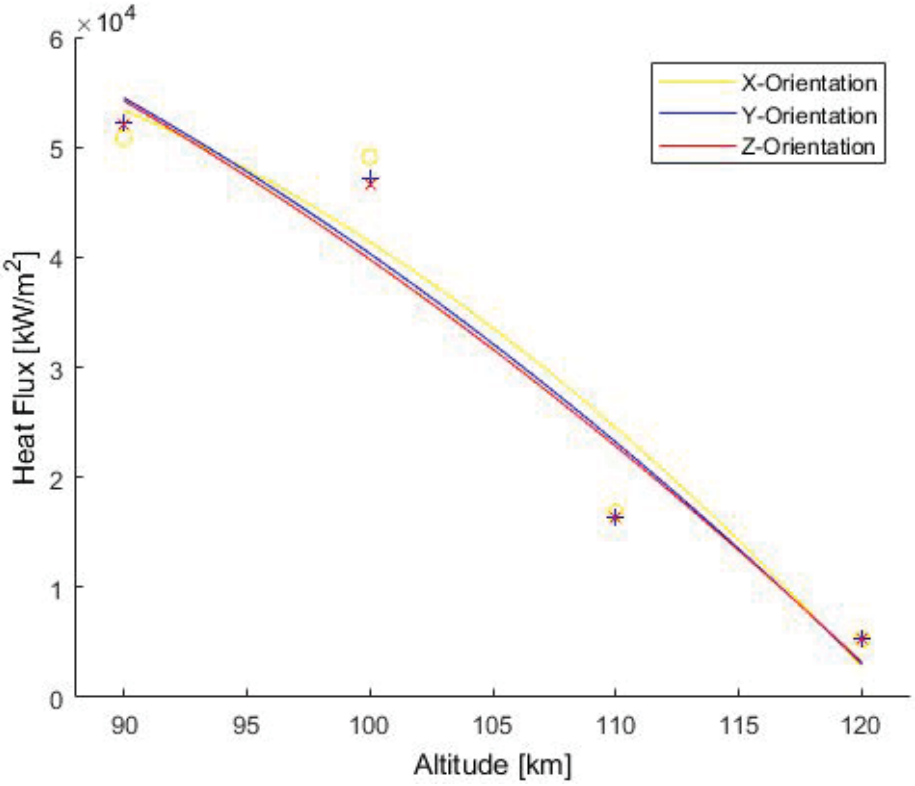

Figure 30. Maximum SPARTA Skip Perigee Heat Flux

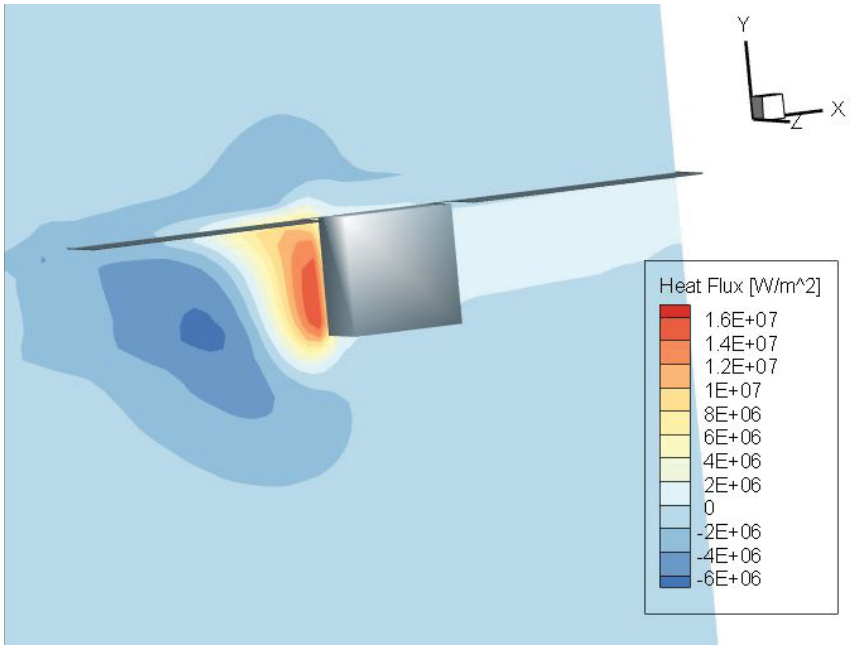

Figure 31. Grid Heat Flux: 110 km, Flow Positive X-Direction

4.3 Comparison of SPARTA Heat Flux with Closed-Form Equation

The closed-form heat flux stagnation point approximation is compared to computational data, shown in the equation below [34]:

$$\dot{Q} = 199,830 \left(\frac{\rho}{\rho_{SL}}\right)^{0.5} \left(\frac{V_R}{V_{SL}}\right)^{3.15} \frac{kW}{m^2} \tag{2.1}$$

Table 9 shows the maximum grid heat flux as compared to the approximate analytical stagnation heat flux for all perigee altitudes. It is apparent that the computational heat flux is two orders of magnitude higher than the analytic heat flux. This makes sense, as the maximum heat flux measured within the flow field will be much greater than the stagnation heat flux infinitely close to the satellite body. For reference, an 1800 kW/m^2 was determined by Tewari as the maximum capsule breakup heat flux [34]; though, this seems low for a *capsule* breakup given the typical material composition of a reentry capsule.

Table 9. Heat Flux Comparison

h_p [km]	Avg Max Grid Heat Flux [kW/m^2]	Analytical Stagnation Heat Flux [kW/m^2]
90	51700	291
100	46700	123
110	16600	54
120	5290	28

4.4 Summary

This chapter investigated the aerothermodynamic parameters at various skip perigee altitudes, with three flow orientations selected for analysis in each altitude case. Force and pressure computational results indicate that a 90-km perigee altitude is likely sur-

vivable for a typical small satellite geometry; based on their power function trends, a continued decrease in altitude would result in a rapid increase in these variables, thus making survivability below 90 km uncertain. Further, the temperature values are within an acceptable range for a reentry scenario, and illustrate an expected decreasing data trend with decreasing altitude. Finally, the maximum flow field heat flux values over h $\in$ [120, 90] km were recorded $\dot{q} \in$ [5290, 51700] kW/m^2.

V. Conclusions and Recommendations

5.1 Research Conclusions

The use of DSMC for general skip trajectories is a valuable method to compute aerothermodynamic quantities over a given geometry. It is more accurate than CFD for skip trajectories due to higher altitudes within the atmosphere with which the trajectories traverse; Knudsen numbers at these higher altitudes typically indicate that DSMC is more accurate for computational analysis.

The SPARTA DSMC results match reasonably well with experimental data. The RAM C-II electron densities, a difficult parameter to simulate, were within one order of magnitude as compared to the experimental data. It would be insightful to run the simulation using SPARTA when a version is released that supports recombination reactions with the fix ambipolar command coded. This should further decrease the variation between the computational data closer and the empirical data.

Finally, it was determined that with adequate energy, a small satellite skip trajectory is likely survivable to an approximate perigee altitude of 90 km. The maximum pressure and force values of 172.6 Pa and 39.3 N, respectively, exerted on the satellite should be able to survive at these altitudes. Both of these profiles indicate an exponentially increasing trend as the altitude decreases, indicating the destructive forces would result at lower altitudes. The satellite's material is also an important factor to consider, with its varying effects on structural integrity, ablation, and burn-up; different materials will safely descend to varying perigee altitudes.

5.2 Research Significance

This research utilized the computational DSMC simulator SPARTA for both the RAM C-II and small satellite analyses. The following is a summary of the research significance:

- First implementation of SPARTA DSMC code at AFIT
- First application of DSMC method to study computational reentry aerothermodynamics at AFIT
- One of the few research applications of DSMC aerothermodynamics for skip entry maneuver
- Identification of baseline aerothermodynamics for a small satellite performing skip entry at its most stressing trajectory state

A review of the research objectives are briefly discussed, written again below for convenience:

- Validate the use of a Direct Simulation Monte Carlo (DSMC) rarefied flow simulator for satellite analysis.
- Explore perigee depth limitations for a generic satellite structural configuration.
- Compare an established reentry heating model to the stagnation heat flux and loading effects at various skip perigee altitudes.
- Determine a range of entry flight path angles that yield a corresponding skip perigee within survivable aerothermodynamic limits.

A validation of the DSMC rarefied flow simulator was satisfactory based on the analysis of the RAM C-II electron densities and stagnation streamline temperature profiles.

The perigee depth limitation was selected at 90 km due to previous research indicating that 85 km is the upper end of the satellite breakup range. A parametric study would have to be accomplished to determine the exact perigee altitude below 90 km prior to breakup. The established reentry heating model was based on stagnation heat flux values, while the data collected during the heat flux analysis was based on maximum flow field values. These quantities will inevitably vary, as the locations of the two heat fluxes differ based on the distance away from the geometry surface. A range of flight-path angles $\gamma_e \in$ [-.01°, -.43°] and velocities V $\in$ [7.914, 7.584] km/s was determined for the x-directed and z-directed flows, corresponding with the skip perigee altitude h $\in$ [120, 90] km. The y-directed flow, with the inclusion of the solar panel surface areas, shows varying results. The flight-path angle magnitude ranges are greater $\gamma_e \in$ [-.01°, -.99°] and the velocities decrease further V $\in$ [7.914, 7.186] for the respective corresponding altitudes h $\in$ [120, 90] km.

5.3 Recommendations for Future Research

Future SPARTA DSMC analysis could be executed with the inclusion of the solar panel surface area for the y-oriented satellite with the perigee velocities and entry flight-path angles presented in Table 6, which are necessary input variables for the DSMC simulation. Additionally, the minimal surface area depth of the solar panel for the x-oriented and z-oriented satellites could be accounted for when solving the skip entry equations of motion to further refine the perigee velocity input parameter, further refining the aerothermodynamic value accuracy. Other recommendations for future analysis include varying satellite bank angle to re-examine its aerothermodynamic effects. Additionally, an increase in complexity of the geometry would reveal more accurate aerothermodynamic parameters as well, potentially altering the attainable perigee altitude. Another factor to consider is the satellite material and chemical

composition, as varying structures have different strengths and melting points, potentially decreasing a survivable perigee altitude. Further, DSMC simulation analysis could be executed for a spaceplane to reveal aerothermodynamic parameters associated with a skip trajectory. Finally, DSMC research on satellite drag effects in $h \in [200, 400]$ km could be accomplished to refine relative orbital motion control.

Appendix A. Coding Scripts

SPARTA

RAM C-II

```
seed              12345
dimension         2
global            gridcut 0.0030 comm/sort yes
boundary          o ar p
create_box        -0.10 1.289999962 0.0 .6 -0.2 0.2
create_grid       1159 500  1
balance_grid      rcb part
global            nrho 3.5184e20 fnum 3.5184e16 weight cell radius
species           air.species N2 O2 N O NO NO+ e
mixture           air_wo_ID N2 O2 N O NO NO+ e vstream 7650. 0. 0. temp 193.
mixture           air_wo_ID N2 frac .79
mixture           air_wo_ID O2 frac .21
mixture           air_wo_ID NO+ e group SELF
mixture           air_wo_ID N2 O2 N O NO group neutrals

mixture           air_ambi_ID N2 O2 N O NO NO+ vstream 7650. 0. 0. temp 193.
mixture           air_ambi_ID N2 frac .79
mixture           air_ambi_ID O2 frac .21

fix               let_particles_flow_ID emit/face air_ambi_ID xlo
collide           vss air_wo_ID air.vss
collide_modify    vibrate smooth ambipolar yes
fix               ambipolar_ID ambipolar e NO+
```

```
react               tce air.tce

read_surf           data.ramc2

surf_collide        surface_coll_ID diffuse 1000 .9
surf_modify         all collide surface_coll_ID
surf_react          SURF prob air.surf
timestep            1e-7

#fix                 refine_me_ID adapt 1000 all refine particle 10 45000000
fix                 balance_particles_ID balance 1000 1.15 rcb part

stats               250
stats_style         step np ncomm tpcpu ncoll nscoll nreact nsreact nsplit

run                 5000

#unfix              refine_me_ID
unfix               balance_particles_ID

run                 15000

compute             computegridID2 grid all species nrho
fix                 species_ID2 ave/grid all 10 20 1000 c_computegridID2[*] ave one
dump                dumpgridID2 grid all 1000 species.* id f_species_ID2[*]
write_grid          parent species.grid
```

```
compute             computegridtempsID grid all air_wo_ID trot tvib erot evib
fix                 species_tempsID ave/grid all 10 20 1000 c_computegridtempsID[*]
                    ave one
dump                dumpgridtempsID grid all 1000 temps.* id f_species_tempsID[*]
write_grid          parent temps.grid

compute             thermalgridID thermal/grid all air_wo_ID temp
fix                 thermal_temp_ID ave/grid all 10 20 1000 c_thermalgridID[*]
                    ave one
dump                dumpgridthermalID grid all 1000 temp.* id f_thermal_temp_ID[*]
write_grid          parent thermal.grid

run                 10000
```

RAM C-II: Reduced Electron Mass

```
seed                12345
dimension           2
global              gridcut 0.0030 comm/sort yes
boundary            o ar p
create_box          -0.10 1.289999962 0.0 .6 -0.2 0.2
create_grid         1159 500  1
balance_grid        rcb part
global              nrho 3.5184e20 fnum 3.5184e16 weight cell radius
species             air.species N2 O2 N O NO NO+ e
mixture             air_wo_ID N2 O2 N O NO NO+ e vstream 7650. 0. 0. temp 193.
mixture             air_wo_ID N2 frac .79
mixture             air_wo_ID O2 frac .21
mixture             air_wo_ID NO+ e group SELF
mixture             air_wo_ID N2 O2 N O NO group neutrals

mixture             air_ambi_ID N2 O2 N O NO NO+ vstream 7650. 0. 0. temp 193.
mixture             air_ambi_ID N2 frac .79
mixture             air_ambi_ID O2 frac .21

fix                 let_particles_flow_ID emit/face air_ambi_ID xlo
collide             vss air_wo_ID air.vss
collide_modify      vibrate smooth ambipolar yes
fix                 ambipolar_ID ambipolar e NO+
react               tce air.tce
```

```
read_surf           data.ramc2

surf_collide        surface_coll_ID diffuse 1000 .9
surf_modify         all collide surface_coll_ID
surf_react          SURF prob air.surf
timestep            1e-7

#fix                 refine_me_ID adapt 1000 all refine particle 10 45000000
fix                 balance_particles_ID balance 1000 1.15 rcb part

stats               250
stats_style         step np ncomm tpcpu ncoll nscoll nreact nsreact nsplit

run                 5000

#unfix              refine_me_ID
unfix               balance_particles_ID

run                 15000

compute             computegridID2 grid all species nrho
fix                 species_ID2 ave/grid all 10 20 1000 c_computegridID2[*] ave one
dump                dumpgridID2 grid all 1000 species.* id f_species_ID2[*]
write_grid          parent species.grid

compute             computegridtempsID grid all air_wo_ID trot tvib erot evib
```

```
fix                 species_tempsID ave/grid all 10 20 1000 c_computegridtempsID[*]
                    ave one
dump                dumpgridtempsID grid all 1000 temps.* id f_species_tempsID[*]
write_grid          parent temps.grid

compute             thermalgridID thermal/grid all air_wo_ID temp
fix                 thermal_temp_ID ave/grid all 10 20 1000 c_thermalgridID[*]
                    ave one
dump                dumpgridthermalID grid all 1000 temp.* id f_thermal_temp_ID[*]
write_grid          parent thermal.grid

run                 10000
```

Satellite Code

```
#90km  Y-Orientation

seed                12345
dimension           3
global              gridcut 0.0 comm/sort yes
boundary            r o r
create_box          -4 4 -4 4 -4 4
create_grid         100 100 100
balance_grid        rcb part
global              nrho 7.087e19 fnum 7.087e17 weight cell volume

species             air.species N2 O2 N O NO NO+ e
mixture             air N2 O2 N O NO NO+ e vstream 0 7584.0 0 temp 184.0
mixture             air N2 frac .79
mixture             air O2 frac .21
mixture             air NO+ e group SELF
mixture             air N2 O2 N O NO group neutrals

mixture             air_ambi_ID N2 O2 N O NO NO+ vstream 0 7584. 0. temp 184.0
mixture             air_ambi_ID N2 frac .79
mixture             air_ambi_ID O2 frac .21

fix                 inX emit/face air_ambi_ID ylo
collide             vss air air.vss
collide_modify      vibrate smooth ambipolar yes
```

```
fix                 ambipolar_ID ambipolar e NO+
react               tce air.tce

read_surf           data.satellite.doesntworkpos

surf_collide        1 diffuse 1000.0 0.9
surf_modify         all collide 1
surf_react          SURF prob air.surf
timestep            3.47e-6

fix                 2 balance 1000 1.25 rcb part

stats               100
stats_style         step cpu np nattempt ncoll nscoll nscheck

run                 5000

unfix               2

run                 15000

compute             1 surf all air press px py pz fx fy fz ke mflux
fix                 1 ave/surf all 1 1000 1000 c_1[*] ave one
dump                1 surf all 1000 surf.* id f_1[*]
write_surf          satellite.surf
```

```
compute             2 grid all species u v w erot trot evib tvib ke
fix                 2 ave/grid all 1 1000 1000 c_2[*] ave one
dump                2 grid all 1000 flow.* id f_2[*]
write_grid          parent satellite.grid

compute             thermalgridID thermal/grid all air temp press
fix                 thermal_temp_ID ave/grid all 1 1000 1000 c_thermalgridID[*]
                    ave one
dump                dumpgridthermalID grid all 1000 temp.* id f_thermal_temp_ID[*]
write_grid          parent thermal.grid

compute             4 eflux/grid all air heatx heaty heatz
fix                 4 ave/grid all 1 1000 1000 c_4[*] ave one
dump                4 grid all 1000 eflux.* id f_4[*]
write_grid          parent eflux.grid

run                 5000
```

```
#100km X-Orientation

seed                12345
dimension           3
global              gridcut 0.0 comm/sort yes
boundary            o r r
create_box          -4 4 -4 4 -4 4
create_grid         100 100 100
balance_grid        rcb part
global              nrho 1.125e19 fnum 1.125e17 weight cell volume

species             air.species N2 O2 N O NO NO+ e
mixture             air N2 O2 N O NO NO+ e vstream 7751.0 0 0 temp 204.0
mixture             air N2 frac .79
mixture             air O2 frac .21
mixture             air NO+ e group SELF
mixture             air N2 O2 N O NO group neutrals

mixture             air_ambi_ID N2 O2 N O NO NO+ vstream 7751. 0. 0. temp 204.0
mixture             air_ambi_ID N2 frac .79
mixture             air_ambi_ID O2 frac .21

fix                 inX emit/face air_ambi_ID xlo
collide             vss air air.vss
collide_modify      vibrate smooth ambipolar yes
fix                 ambipolar_ID ambipolar e NO+
```

```
react               tce air.tce

read_surf           data.satellite.doesntworkpos

surf_collide        1 diffuse 1000.0 0.9
surf_modify         all collide 1
surf_react          SURF prob air.surf
timestep            3.47e-6

fix                 2 balance 1000 1.25 rcb part

stats               100
stats_style         step cpu np nattempt ncoll nscoll nscheck

run                 5000

unfix               2

run                 15000

compute             1 surf all air press px py pz fx fy fz ke mflux
fix                 1 ave/surf all 1 1000 1000 c_1[*] ave one
dump                1 surf all 1000 surf.* id f_1[*]
write_surf          satellite.surf

compute             2 grid all species u v w erot trot evib tvib ke
```

```
fix                 2 ave/grid all 1 1000 1000 c_2[*] ave one
dump                2 grid all 1000 flow.* id f_2[*]
write_grid          parent satellite.grid

compute             thermalgridID thermal/grid all air temp press
fix                 thermal_temp_ID ave/grid all 1 1000 1000 c_thermalgridID[*]
                    ave one
dump                dumpgridthermalID grid all 1000 temp.* id f_thermal_temp_ID[*]
write_grid          parent thermal.grid

compute             4 eflux/grid all air heatx heaty heatz
fix                 4 ave/grid all 1 1000 1000 c_4[*] ave one
dump                4 grid all 1000 eflux.* id f_4[*]
write_grid          parent eflux.grid

run                 5000
```

```
#110km Z-Orientation

seed                12345
dimension           3
global              gridcut 0.0 comm/sort yes
boundary            r r o
create_box          -4 4 -4 4 -4 4
create_grid         100 100 100
balance_grid        rcb part
global              nrho 2.182e18 fnum 2.182e16 weight cell volume

species             air.species N2 O2 N O NO NO+ e
mixture             air N2 O2 N O NO NO+ e vstream 0 0 7841.0 temp 266.0
mixture             air N2 frac .79
mixture             air O2 frac .21
mixture             air NO+ e group SELF
mixture             air N2 O2 N O NO group neutrals

mixture             air_ambi_ID N2 O2 N O NO NO+ vstream 0 0 7841.0 temp 266.0
mixture             air_ambi_ID N2 frac .79
mixture             air_ambi_ID O2 frac .21

fix                 inX emit/face air_ambi_ID zlo
collide             vss air air.vss
collide_modify      vibrate smooth ambipolar yes
fix                 ambipolar_ID ambipolar e NO+
```

```
react               tce air.tce

read_surf           data.satellite.doesntworkpos

surf_collide        1 diffuse 1000.0 0.9
surf_modify         all collide 1
surf_react          SURF prob air.surf
timestep            3.47e-6

fix                 2 balance 1000 1.25 rcb part

stats               100
stats_style         step cpu np nattempt ncoll nscoll nscheck

run                 5000

unfix               2

run                 15000

compute             1 surf all air press px py pz fx fy fz ke mflux
fix                 1 ave/surf all 1 1000 1000 c_1[*] ave one
dump                1 surf all 1000 surf.* id f_1[*]
write_surf          satellite.surf

compute             2 grid all species u v w erot trot evib tvib ke
```

```
fix                 2 ave/grid all 1 1000 1000 c_2[*] ave one
dump                2 grid all 1000 flow.* id f_2[*]
write_grid          parent satellite.grid

compute             thermalgridID thermal/grid all air temp press
fix                 thermal_temp_ID ave/grid all 1 1000 1000 c_thermalgridID[*]
                    ave one
dump                dumpgridthermalID grid all 1000 temp.* id f_thermal_temp_ID[*]
write_grid          parent thermal.grid

compute             4 eflux/grid all air heatx heaty heatz
fix                 4 ave/grid all 1 1000 1000 c_4[*] ave one
dump                4 grid all 1000 eflux.* id f_4[*]
write_grid          parent eflux.grid

run                 5000
```

```
#120km X-Orientation

seed                12345
dimension           3
global              gridcut 0.0 comm/sort yes
boundary            o r r
create_box          -4 4 -4 4 -4 4
create_grid         100 100 100
balance_grid        rcb part
global              nrho 5.772e17 fnum 5.772e15 weight cell volume

species             air.species N2 O2 N O NO NO+ e
mixture             air N2 O2 N O NO NO+ e vstream 7914.0 0 0 temp 381.0
mixture             air N2 frac .79
mixture             air O2 frac .21
mixture             air NO+ e group SELF
mixture             air N2 O2 N O NO group neutrals

mixture             air_ambi_ID N2 O2 N O NO NO+ vstream 7914. 0. 0. temp 381.0
mixture             air_ambi_ID N2 frac .79
mixture             air_ambi_ID O2 frac .21

fix                 inX emit/face air_ambi_ID xlo
collide             vss air air.vss
collide_modify      vibrate smooth ambipolar yes
fix                 ambipolar_ID ambipolar e NO+
```

```
react               tce air.tce

read_surf           data.satellite.doesntworkpos

surf_collide        1 diffuse 1000.0 0.9
surf_modify         all collide 1
surf_react          SURF prob air.surf
timestep            3.47e-6

fix                 2 balance 1000 1.25 rcb part

stats               100
stats_style         step cpu np nattempt ncoll nscoll nscheck

run                 5000

unfix               2

run                 15000

compute             1 surf all air press px py pz fx fy fz ke mflux
fix                 1 ave/surf all 1 1000 1000 c_1[*] ave one
dump                1 surf all 1000 surf.* id f_1[*]
write_surf          satellite.surf

compute             2 grid all species u v w erot trot evib tvib ke
```

```
fix                 2 ave/grid all 1 1000 1000 c_2[*] ave one
dump                2 grid all 1000 flow.* id f_2[*]
write_grid          parent satellite.grid

compute             thermalgridID thermal/grid all air temp press
fix                 thermal_temp_ID ave/grid all 1 1000 1000 c_thermalgridID[*]
                    ave one
dump                dumpgridthermalID grid all 1000 temp.* id f_thermal_temp_ID[*]
write_grid          parent thermal.grid

compute             4 eflux/grid all air heatx heaty heatz
fix                 4 ave/grid all 1 1000 1000 c_4[*] ave one
dump                4 grid all 1000 eflux.* id f_4[*]
write_grid          parent eflux.grid

run                 5000
```

MATLAB

Calculation of x/D Location of Reflectometer

```
clc;
D=.3048;    %diameter is in meters, (30.48cm)

% x/D=.15
x=D*.15;
disp([‘x/D=.15   x= ’, num2str(x)]);

% x/D=.76
x=D*.76;
disp([‘x/D=.76   x= ’, num2str(x)]);

% x/D=2.3
x=D*2.3;
disp([‘x/D=2.3   x= ’, num2str(x)]);

% x/D=3.48
x=D*3.48;
disp([‘x/D=3.48  x= ’, num2str(x)]);
```

RAM C-II Mean Free Path @ Stagnation Point

```
clc; clear

Tref=273;           %kelvin
Ttr_avg=2.5e3;

w=.74;
k=1.38e-23;
d=4.17e-10;         %HARD SPHERE - VHS (see pg 243 non-equilibrium txt, Reference 11)
sigma=.42e-18;      %collisional cross section from website (avg of N2 and O2)
v=w-1/2;

% at 81 km;
nrho=1.35e21;

Av=6.022140857e23; %mol^-1
molar_mass_N2=28.013;  %grams/mol
molar_mass_O2=15.999;  %grams/mol
mass_N2_grams=molar_mass_N2/Av;   %grams
mass_O2_grams=molar_mass_O2/Av;   %grams
mass_N2=mass_N2_grams*1e-3;   %kg
mass_O2=mass_O2_grams*1e-3;   %kg

mfp85_non_equilibrium_txt=1/(sqrt(2)*nrho*pi*d^2);
mfp85=(1/(sqrt(2)*nrho*pi*d^2))*((Ttr_avg/Tref)^v);
```

```
mfp85_N2=(1/(sqrt(mass_N2/mass_O2)*nrho*pi*d^2))*((Ttr_avg/Tref)^v);
%calculating mfp of Nitrogen (N2) actually uses the mass ratio in the sqrt
mfp85_O2=(1/(sqrt(mass_O2/mass_N2)*nrho*pi*d^2))*((Ttr_avg/Tref)^v);
%calculating mfp of Oxygen (O2) actually uses the mass ratio in the sqrt
mfp85_averaged_masses=(mfp85_N2+mfp85_O2)/2;
%mfp with temp ratio and accounting for actual masses
%taking the mfp of N2 and then O2 and finding avg

%Calculating the box dimensions
x=1.389999962/(1/2*mfp85_averaged_masses);
y=.6/(1/2*mfp85_averaged_masses);



% MEAN COLLISSION TIME @ the stagnation point
k=1.38065e-23;   %Boltzmann Constatn - see p154txt - reference 11
m_r=(mass_N2*mass_O2)/(mass_N2+mass_O2); %reduced mass
%see formula p 23 and 335 txt - refernce 11

Tcoll=1/((Ttr_avg/Tref)^(1/2-v)*2*nrho*d^2*sqrt((2*pi*k*Tref)/m_r));
```

Normal Line to Surface of RAM C-II Probe Locations

```
clc; clear;
% -.37 along x is where we are saying the body starts

% Pt 0: .045 meters along payload
x1_0=-.325;
y1_0=.187;
L=.25;
x2_0=x1_0-(L*sind(29.33));
y2_0=y1_0+(L*cosd(29.33));

% Pt 1: .23 meters along payload
x1_1=-.14;
y1_1=.31;
L=.35;
x2_1=x1_1-(L*sind(9));
y2_1=y1_1+(L*cosd(9));

% Pt2: .70 meters along payload
x1_2=.33;
y1_2=.43;
L=.5;
x2_2=x1_2-(L*sind(9));
y2_2=y1_2+(L*cosd(9));

% Pt3: 1.06 meters along payload
```

```
x1_3=.69;

y1_3=.52;

L=.5;

x2_3=x1_3-(L*sind(9));

y2_3=y1_3+(L*cosd(9));
```

Chemical Reaction Constants

```
%Converting Cf to A for Sparta ‘‘air.tce’’ File
%Cf and A are both constants in the eq on pg 268 sparta manual
%and p231 vincenti &kruger physical gas dynamics
clc; clear;

avo= 6.02214e23;  %Avogadro’s number

Cf=1.5e18;  %(cm^3 mol^-1 sec^-1) %see Vinceti&Kruger’s Physical Gas Dynamics p231
A_cm=Cf/avo;  %still in cm
A=A_cm*1e-6;  %this is the form we want for SPARTA (in meters)
```

RAM C-II- Finding the X-distance (m) off the Nose

```
%the equation is Z/Rn=#


clc; clear;

Rn=.1524;


% -.1      (x/Rn's value = -.1 of the x-axis in the plots)

x1=Rn*-.1;


% -.2 meters

x2=Rn*-.2;


% -.3 meters

x3=Rn*-.3;


% -.4 meters

x4=Rn*-.4;


% -.5 meters

x5=Rn*-.5;


% -.6 meters

x6=Rn*-.6;
```

```
%finding where x/Rn=-.1, x/Rn=-.2, etc. lies on tecplot simulation domain x-axis.
% SIDE NOTE: THE BODY STARTS AT -.37 METERS
start=-.37;

%Finding x/Rn=-.1
neg_point_one=start+x1;

%Finding x/Rn=-.2
neg_point_two=start+x2;

%Finding x/Rn=-.3
neg_point_three=start+x3;

%Finding x/Rn=-.4
neg_point_four=start+x4;

%Finding x/Rn=-.5
neg_point_five=start+x5;

%Finding x/Rn=-.6
neg_point_six=start+x6;
```

Satellite Mean Free Path

```
clc; clear

Tref=273;           %kelvin
Ttr_avg=21614;

w=.74;
k=1.38e-23;
d=4.17e-10;         %HARD SPHERE - VHS (see pg 243 txt)
sigma=.42e-18;      %collisional cross section from website (avg of N2 and O2)
v=w-1/2;

nrho=1.35e21;

Av=6.022140857e23; %mol^-1
molar_mass_N2=28.013;  %grams/mol
molar_mass_O2=15.999;  %grams/mol
mass_N2_grams=molar_mass_N2/Av;   %grams
mass_O2_grams=molar_mass_O2/Av;   %grams
mass_N2=mass_N2_grams*1e-3;   %kg
mass_O2=mass_O2_grams*1e-3;   %kg

mfp85_non_equilibrium_txt=1/(sqrt(2)*nrho*pi*d^2);
mfp85=(1/(sqrt(2)*nrho*pi*d^2))*((Ttr_avg/Tref)^v);
%mfp with temp ratio (sqrt(2) term included)
```

```
mfp85_N2=(1/(sqrt(mass_N2/mass_O2)*nrho*pi*d^2))*((Ttr_avg/Tref)^v);
%calculating mfp of Nitrogen (N2) actually uses the mass ratio in the sqrt
mfp85_O2=(1/(sqrt(mass_O2/mass_N2)*nrho*pi*d^2))*((Ttr_avg/Tref)^v);
%calculating mfp of Oxygen (O2) actually uses the mass ratio in the sqrt
mfp85_averaged_masses=(mfp85_N2+mfp85_O2)/2;
%mfp with temp ratio and accounting for actual masses-
%taking the mfp of N2 and then O2 and finding avg

%Calculating the box dimensions
x=6/(1*mfp85_averaged_masses);
y=6/(1/2*mfp85_averaged_masses);


% MEAN COLLISSION TIME @ the stagnation point
k=1.38065e-23;   %Boltzmann Constatn - see p154 bott of non equilibrium txt
m_r=(mass_N2*mass_O2)/(mass_N2+mass_O2);      %reduced mass
%see formula p 23 and 335 txt

Tcoll=1/((Ttr_avg/Tref)^(1/2-v)*2*nrho*d^2*sqrt((2*pi*k*Tref)/m_r));
```

Ambient Satellite Mean Free Path

```
%90km



clc; clear


Tref=273;           %kelvin
Ttr_avg=184;


w=.74;
k=1.38e-23;
d=4.17e-10;
sigma=.42e-18;
v=w-1/2;


nrho=7.087e19;
Av=6.022140857e23; %mol^-1
molar_mass_N2=28.013;  %grams/mol
molar_mass_O2=15.999;  %grams/mol
mass_N2_grams=molar_mass_N2/Av;   %grams
mass_O2_grams=molar_mass_O2/Av;   %grams
mass_N2=mass_N2_grams*1e-3;   %kg
mass_O2=mass_O2_grams*1e-3;   %kg


mfp85_non_equilibrium_txt=1/(sqrt(2)*nrho*pi*d^2);
mfp85=(1/(sqrt(2)*nrho*pi*d^2))*((Ttr_avg/Tref)^v);
```

```
mfp85_N2=(1/(sqrt(mass_N2/mass_O2)*nrho*pi*d^2))*((Ttr_avg/Tref)^v);
mfp85_O2=(1/(sqrt(mass_O2/mass_N2)*nrho*pi*d^2))*((Ttr_avg/Tref)^v);
mfp85_averaged_masses=(mfp85_N2+mfp85_O2)/2;

%Calculating the box dimensions
x=6/(1*mfp85_averaged_masses);
y=6/(1/2*mfp85_averaged_masses);


% MEAN COLLISSION TIME @ the stagnation point
k=1.38065e-23;
m_r=(mass_N2*mass_O2)/(mass_N2+mass_O2);
Tcoll=1/((Ttr_avg/Tref)^(1/2-v)*2*nrho*d^2*sqrt((2*pi*k*Tref)/m_r));
```

```
%100km



clc; clear

Tref=273;           %kelvin
Ttr_avg=204;

w=.74;
k=1.38e-23;
d=4.17e-10;
sigma=.42e-18;
v=w-1/2;

nrho=1.125e19;

Av=6.022140857e23; %mol^-1
molar_mass_N2=28.013;  %grams/mol
molar_mass_O2=15.999;  %grams/mol
mass_N2_grams=molar_mass_N2/Av;   %grams
mass_O2_grams=molar_mass_O2/Av;   %grams
mass_N2=mass_N2_grams*1e-3;   %kg
mass_O2=mass_O2_grams*1e-3;   %kg

mfp85_non_equilibrium_txt=1/(sqrt(2)*nrho*pi*d^2);
mfp85=(1/(sqrt(2)*nrho*pi*d^2))*((Ttr_avg/Tref)^v);
```

```
mfp85_N2=(1/(sqrt(mass_N2/mass_O2)*nrho*pi*d^2))*((Ttr_avg/Tref)^v);
mfp85_O2=(1/(sqrt(mass_O2/mass_N2)*nrho*pi*d^2))*((Ttr_avg/Tref)^v);
mfp85_averaged_masses=(mfp85_N2+mfp85_O2)/2;

%Calculating the box dimensions
x=6/(1*mfp85_averaged_masses);
y=6/(1/2*mfp85_averaged_masses);


% MEAN COLLISSION TIME @ the stagnation point
k=1.38065e-23;
m_r=(mass_N2*mass_O2)/(mass_N2+mass_O2);

Tcoll=1/((Ttr_avg/Tref)^(1/2-v)*2*nrho*d^2*sqrt((2*pi*k*Tref)/m_r));
```

```
%110km



clc; clear

Tref=273;           %kelvin
Ttr_avg=266;

w=.74;
k=1.38e-23;
d=4.17e-10;
sigma=.42e-18;
v=w-1/2;

nrho=2.182e18;

Av=6.022140857e23; %mol^-1
molar_mass_N2=28.013;  %grams/mol
molar_mass_O2=15.999;  %grams/mol
mass_N2_grams=molar_mass_N2/Av;   %grams
mass_O2_grams=molar_mass_O2/Av;   %grams
mass_N2=mass_N2_grams*1e-3;   %kg
mass_O2=mass_O2_grams*1e-3;   %kg

mfp85_non_equilibrium_txt=1/(sqrt(2)*nrho*pi*d^2);
mfp85=(1/(sqrt(2)*nrho*pi*d^2))*((Ttr_avg/Tref)^v);
```

```
mfp85_N2=(1/(sqrt(mass_N2/mass_O2)*nrho*pi*d^2))*((Ttr_avg/Tref)^v);
mfp85_O2=(1/(sqrt(mass_O2/mass_N2)*nrho*pi*d^2))*((Ttr_avg/Tref)^v);
mfp85_averaged_masses=(mfp85_N2+mfp85_O2)/2;

%Calculating the box dimensions
x=6/(1*mfp85_averaged_masses);
y=6/(1/2*mfp85_averaged_masses);


% MEAN COLLISSION TIME @ the stagnation point
k=1.38065e-23;
m_r=(mass_N2*mass_O2)/(mass_N2+mass_O2);

Tcoll=1/((Ttr_avg/Tref)^(1/2-v)*2*nrho*d^2*sqrt((2*pi*k*Tref)/m_r));
```

```
%120km



clc; clear

Tref=273;           %kelvin
Ttr_avg=381;

w=.74;
k=1.38e-23;
d=4.17e-10;
sigma=.42e-18;
v=w-1/2;

nrho=5.772e17;

Av=6.022140857e23; %mol^-1
molar_mass_N2=28.013;  %grams/mol
molar_mass_O2=15.999;  %grams/mol
mass_N2_grams=molar_mass_N2/Av;   %grams
mass_O2_grams=molar_mass_O2/Av;   %grams
mass_N2=mass_N2_grams*1e-3;   %kg
mass_O2=mass_O2_grams*1e-3;   %kg

mfp85_non_equilibrium_txt=1/(sqrt(2)*nrho*pi*d^2);
mfp85=(1/(sqrt(2)*nrho*pi*d^2))*((Ttr_avg/Tref)^v);
```

```
mfp85_N2=(1/(sqrt(mass_N2/mass_O2)*nrho*pi*d^2))*((Ttr_avg/Tref)^v);
mfp85_O2=(1/(sqrt(mass_O2/mass_N2)*nrho*pi*d^2))*((Ttr_avg/Tref)^v);
mfp85_averaged_masses=(mfp85_N2+mfp85_O2)/2;

%Calculating the box dimensions
x=6/(1*mfp85_averaged_masses);
y=6/(1/2*mfp85_averaged_masses);


% MEAN COLLISSION TIME @ the stagnation point
k=1.38065e-23;
m_r=(mass_N2*mass_O2)/(mass_N2+mass_O2);

Tcoll=1/((Ttr_avg/Tref)^(1/2-v)*2*nrho*d^2*sqrt((2*pi*k*Tref)/m_r));
```

Satellite Heat Flux

```
clc;clear;close all;


%90km Perigee


rho=3.396e-6; %kg/m^3
rho_sl=1.225; %kg/m^3
V_R=7584; %m/s
mu=398600.442e9; %m^3/s^2
R_earth=6378137; %m
V_sl=sqrt(mu/R_earth);
Qdot=199830*(rho/rho_sl)^.5*(V_R/V_sl)^3.15;



%100km Perigee


rho2=5.297e-7; %kg/m^3
rho_sl2=1.225; %kg/m^3
V_R2=7751; %m/s
mu2=398600.442e9; %m^3/s^2
R_earth2=6378137; %m
V_sl2=sqrt(mu2/R_earth2);
Qdot2=199830*(rho2/rho_sl2)^.5*(V_R2/V_sl2)^3.15;



%110km Perigee
```

```
rho3=9.661e-8; %kg/m^3

rho_sl3=1.225; %kg/m^3

V_R3=7841; %m/s

mu3=398600.442e9; %m^3/s^2

R_earth3=6378137; %m

V_sl3=sqrt(mu3/R_earth3);

Qdot3=199830*(rho3/rho_sl3)^.5*(V_R3/V_sl3)^3.15;



%120km Perigee

rho4=2.438e-8; %kg/m^3

rho_sl4=1.225; %kg/m^3

V_R4=7914; %m/s

mu4=398600.442e9; %m^3/s^2

R_earth4=6378137; %m

V_sl4=sqrt(mu4/R_earth4);

Qdot4=199830*(rho4/rho_sl4)^.5*(V_R4/V_sl4)^3.15;
```

Electron Density Plots

```
clc; clear; close all;

hf = figure; %Open figure and keep handle
hf=colordef(hf,'white'); %Set color scheme
hf.Color='w'; %Set background color of figure window

%fnum 3.52e16
y=[3.3e19, 5.27e18, 1.84e18, 1.75e18];
x=[.045, .23, .70, 1.06];
%semilogy(x,y)
scatter(x,y)
set(gca,'yscale','log')
hold on

%fnum 3.4e16 & recombination reaction NO+ & electron mass 9.11e-28
y6=[6.5e18, 8.8e17, 3e17, 2.8e17];
x6=[.045, .23, .70, 1.06];
%semilogy(x2,y2)
scatter(x6,y6)
set(gca,'yscale','log')

%NASA DATA
y2=[6.3e17, 3.5e16, 1.2e16, 7.5e15];
x2=[.045, .23, .70, 1.06];
%semilogy(x2,y2)
```

```
scatter(x2,y2,‘y’)
set(gca,‘yscale’,‘log’)

ylabel(‘Electron Number Density [m^{-3}]’)
xlabel(‘Distance along RAM C-II Body [m]’)

legend(‘SPARTA Simulation: Ambipolar’, ‘SPARTA Simulation: Recombination’,...
‘RAM C-II Experimental Data’)
```

Satellite Pressure Plots

```
clc;clear;close all;
hf = figure; %Open figure and keep handle
hf=colordef(hf,'white'); %Set color scheme
hf.Color='w'; %Set background color of figure window

% X Orientation
x=[90, 100, 110, 120];
y=[155.8, 20.2, 3.8, 1.0];
scatter(x,y,'y');
hold on
x_=linspace(90,120,1000);
y_=3e36.*x_.^(-17.59);
a=plot(x_,y_,'y');
hold on

% Y Orientation
x2=[90, 100, 110, 120];
y2=[91.5, 14.2, 2.8, .8];
scatter(x2,y2,'b','+')
hold on
x2_=linspace(90,120,1000);
y2_=2e34.*x_.^(-16.56);
b=plot(x2_,y2_,'b');
hold on
```

```
% Z Orientation
x3=[90, 100, 110, 120];
y3=[172.6, 21.5, 3.9, 1.0];
scatter(x3,y3,‘r’,‘x’)
hold on
x3_=linspace(90,120,1000);
y3_=1.8430999545674e37.*x_.^(-17.94);
c=plot(x3_,y3_,‘r’);
hold on

xlim([88 122])
xlabel(‘Altitude [km]’)
ylabel(‘Pressure [Pa]’)
legend([a b c],‘X-Orientation’,‘Y-Orientation’,‘Z-Orientation’,...
‘location’,‘best’)
```

Satellite Force Plots

```
clc;clear;close all;
hf = figure; %Open figure and keep handle
hf=colordef(hf,'white'); %Set color scheme
hf.Color='w'; %Set background color of figure window

% X Orientation
x=[90, 100, 110, 120];
y=[12.9, 2.2, .44, .13];
scatter(x,y,'y');
hold on
x_=linspace(90,120,1000);
y_=4e32.*x_.^(-16.1);
a=plot(x_,y_,'y');
hold on

% Y Orientation
x2=[90, 100, 110, 120];
y2=[39.3, 6.6, 1.37, .39];
scatter(x2,y2,'b','+')
hold on
x2_=linspace(90,120,1000);
y2_=7e32.*x_.^(-16.01);
b=plot(x2_,y2_,'b');
hold on
```

```
% Z Orientation
x3=[90, 100, 110, 120];
y3=[23.9, 4.0, .82, .23];
scatter(x3,y3,'r','x')
hold on
x3_=linspace(90,120,1000);
y3_=1e33.*x_.^(-16.21);
c=plot(x3_,y3_,'r');
hold on

xlim([88 122])
xlabel('Altitude [km]')
ylabel('Force [N]')
legend([a b c],'X-Orientation','Y-Orientation',...
'Z-Orientation')
```

Satellite Heat Flux Plots

```
clc;clear;close all;
hf = figure; %Open figure and keep handle
hf=colordef(hf,'white'); %Set color scheme
hf.Color='w'; %Set background color of figure window

% X Orientation
x=[90, 100, 110, 120];
y=[50800, 49100, 16800, 5278];
a=scatter(x,y,'y');
hold on
x_=linspace(90,120,1000);
y_=-24.555.*x_.^2 + 3467.9.*x_ - 59846;
% y_=4e20.*x_.^(-8.078)
a=plot(x_,y_,'y');
hold on

% Y Orientation
x2=[90, 100, 110, 120];
y2=[52200, 47100, 16400, 5280];
b=scatter(x2,y2,'b','+')
hold on
x2_=linspace(90,120,1000);
y2_=-15.05.*x2_.^2 + 1445.9*x2_ + 46233;
b=plot(x2_,y2_,'b');
hold on
```

```
% Z Orientation
x3=[90, 100, 110, 120];
y3=[52100, 46700, 16400, 5280];
c=scatter(x3,y3,‘r’,‘x’)
hold on
x3_=linspace(90,120,1000);
y3_=-13.*x3_.^2 + 1030.*x3_ + 66800;
c=plot(x3_,y3_,‘r’);
hold on

xlim([88 122])
xlabel(‘Altitude [km]’)
ylabel(‘Heat Flux [kW/m^{2}]’)
legend([a b c],‘X-Orientation’,‘Y-Orientation’,...
‘Z-Orientation’)
```

Satellite Temperature Plots

```
clc;clear;close all;
hf = figure; %Open figure and keep handle
hf=colordef(hf,'white'); %Set color scheme
hf.Color='w'; %Set background color of figure window

% X Orientation
x=[90, 100, 110, 120];
y=[21500, 25180, 25200, 26000];
scatter(x,y,'y');
hold on
x_=linspace(90,120,1000);
y_=0.74.*x_.^3 - 240.3.*x_.^2 + 25971.*x_ - 908920;
% y_=-7.2.*x_.^2 + 1647.2.*x_ - 68206;
a=plot(x_,y_,'y');
hold on

% Y Orientation
x2=[90, 100, 110, 120];
y2=[22800, 26220, 26680, 27370];
scatter(x2,y2,'b','+');
hold on
x2_=linspace(90,120,1000);
y2_=0.5317.*x2_.^3 - 174.3.*x2_.^2 + 19051.*x2_ - 667530;
% y2_=-6.825.*x2_.^2 + 1575.*x2_ - 63503;
b=plot(x2_,y2_,'b');
```

```
hold on

% Z Orientation
x3=[90, 100, 110, 120];
y3=[21800, 26100, 26300, 27100];
scatter(x3,y3,'r','x')
hold on
x3_=linspace(90,120,1000);
y3_=0.7833.*x3_.^3 - 255.5.*x3_.^2 + 27747.*x3_ - 976900;
% y3_=-8.75.*x3_.^2 + 1998.5.*x3_ - 86955;
c=plot(x3_,y3_,'r');
hold on

xlim([88 122])
xlabel('Altitude [km]')
ylabel('Temperature [K]')
legend([a b c],'X-Orientation','Y-Orientation','Z-Orientation',...
'location','best')
```

"Fig 19: RAM C-II DSMC Stagnation Line Temperatures" Code

```
clc; close all;
hf = figure; %Open figure and keep handle
hf=colordef(hf,'white'); %Set color scheme
hf.Color='w'; %Set background color of figure window
plot(Boyd1(:,1),Boyd1(:,2),'r--',Boyd2(:,1),Boyd2(:,2),'g--',...
Boyd3(:,1),Boyd3(:,2),'b--')
ax = gca
ax.YAxis.Exponent = 0;
hold on
plot(Shevyrin1(:,1),Shevyrin1(:,2),'r:',Shevyrin2(:,1),Shevyrin2(:,2),'g:',...
Shevyrin3(:,1),Shevyrin3(:,2),'b:')
ax = gca
ax.YAxis.Exponent = 0;
hold on
plot(SPARTA1(:,1),SPARTA1(:,2),'r-',SPARTA2(:,1),SPARTA2(:,2),'g-',...
SPARTA3(:,1),SPARTA3(:,2),'b-')
ax = gca
ax.YAxis.Exponent = 0;
ylabel('Temperature [K]')
xlabel('x/R_N')

legend('Boyd T_t', 'Boyd T_r','Boyd T_v', 'Shevyrin T_t',...
'Shevyrin T_v', 'Shevyrin T_t','SPARTA T_t','SPARTA T_r',...
'SPARTA T_v','location','best')
```

Windows: Command Line Code

Converts SPARTA's Output files from Ascii to Binary

```
@echo OFF
  for /f %%a in (‘dir /b OUTPUT*.plt’) do (
  @echo %%~na
  ren %%~na.plt %%~na.tec
  @Preplot %%~na.tec
)
```

Bibliography

[1] S. D'Souza and N. Sarigul-Klijn, "An Analytical Approach to Skip Earth Entry Guidance of a Low L/D Vehicle," *46th AIAA Aerospace Sciences Meeting and Exhibit*, No. 230, January, 2008, pp. 1–13.

[2] P. Lu, C. W. Brunner, S. J. Stachowiak, G. F. Mendeck, M. A. Tigges, and C. J. Cerimele, "Verification of a Fully Numerical Entry Guidance Algorithm," *Journal of Guidance, Control, and Dynamics*, Vol. 40, No. 2, 2017, pp. 230–247.

[3] C. Zhang and T. E. Schwartzentruber, "Robust Cut-Cell Algorithms for DSMC Implementations Employing Multi-Level Cartesian Grids," *Computers and Fluids*, Vol. 69, 2012, pp. 122–135.

[4] G. J. LeBeau and F. E. Lumpkin, "Application Highlights of the DSMC Analysis Code (DAC) Software for Simulating Rarefied Flows," *Computer Methods in Applied Mechanics and Engineering*, Vol. 191, No. 6-7, 2001, pp. 595–609.

[5] J. Evans, P. Huber, and C. Schexnayder, "Calculated Radio Attenuation Due to Plasma Sheath Hypersonic Blunt-Nosed Cone," Technical Report, National Aeronautics and Space Administration Langley Research Center, Hampton, VA, 1963.

[6] K. Hicks, *Introduction to Astrodynamic Reentry*. First Edition, 2009.

[7] M. Tigges, T. Crull, J. Rea, and W. Johnson, "Numerical Skip-Entry Guidance," *American Astronautical Society, Rocky Mountain Section*, Vol. 1, AAS 06, 2018.

[8] E. Mabrouk and B. Dunbar, "What are SmallSats and CubeSats?," National Aeronautics and Space Administration, 7 August 2017; https://www.nasa.gov/content/what-are-smallsats-and-cubesats

[9] I. Boyd and S. Thomas, *Nonequilibrium Gas Dynamics and Molecular Simulation*. Cambridge, United Kingdom: Cambridge University Press, 2017.

[10] M. Gallis and S. Plimpton, "SPARTA Direct Simulation Monte Carlo Simulator," 2018.

[11] R. R. Bate, D. D. Mueller, and J. E. White, *Fundamentals of Astrodynamics*. New York, NY: Dover Publications, Inc., 1971.

[12] R. A. Bettinger and J. T. Black, "Comparative Study of Phasing, Atmospheric Skip Entry, and Simple Plane Change Maneuvers," *Journal of Spacecraft and Rockets*, Vol. 51, No. 6, 2014, pp. 1965–1975,.

[13] C. L. Darby and A. V. Rao, "Optimal Impulsive LEO-to-LEO Multiple-Pass Aeroassisted Orbital Transfer for Small Spacecraft," *Advances in the Astronautical Sciences*, Vol. 136, 2010, pp. 39–52.

[14] A. G. Klothakis, I. K. Nikolos, T. P. Koehler, M. A. Gallis, and S. J. Plimpton, "Validation Simulations of the DSMC Code SPARTA," *AIP Conference Proceedings*, Vol. 1786, 2016.

[15] B. Dunbar, "Mars Exploration Program & Missions: Mars Pathfinder," National Aeronautics and Space Administration; https://mars.nasa.gov/programmissions/missions/past/pathfinder/

[16] R. C. Palharini, C. White, T. J. Scanlon, R. E. Brown, M. K. Borg, and J. M. Reese, "Benchmark Numerical Simulations of Rarefied Non-Reacting Gas Flows Using an Open-Source DSMC Code," *Computers and Fluids*, Vol. 120, 2015, pp. 140–157.

[17] I. D. Boyd, "Direct Simulation Monte Carlo for Atmospheric Entry Code Development and Application Results," *Non-Equilibrium Gas Dynamics From Physical Models to Hypersonic Flights*, Vol. 16, No. 2, 2009.

[18] J. Ryba and B. Dunbar, "Space Shuttle Mission Archives STS-82," National Aeronautics and Space Administration, 23 November 2007; https://www.nasa.gov/mission_pages/shuttle/shuttlemissions/archives/sts-82.html

[19] L. Jones and A. Cross, "Electrostatic-Probe Measurements of Plasma Parameters for Two Reentry Flight Experiments at 25000 Feet per Second," Technical Report, National Aeronautics and Space Administration Langley Research Center, Hampton, VA, 1972.

[20] H. B. Singh, "Composition, Chemistry, and Climate of the Atmosphere," Contractor Technical Report NASA-CR-199355, National Aeronautics and Space Administration, A Division of International Publishing Inc, 2018.

[21] C. Park, *Nonequilibrium Hypersonic Aerothermodynamics*. New York, NY: John Wiley & Sons, 1990.

[22] M. Kizilyalli, J. Corish, and R. Metselaar, "Definitions of Terms for Diffusion in the Solid State (IUPAC Recommendations 1999)," *Pure and Applied Chemistry*, Vol. 71, No. 7, 1999, pp. 1307–1325.

[23] M. A. Gallis, S. J. Plimpton, and S. D. Team, "SPARTA Users' Manual," 2011.

[24] I. D. Boyd, "Modeling of Plasma Formation in Rarefied Hypersonic Entry Flows," *45th AIAA Aerospace Sciences Meeting and Exhibit, AIAA-2007-206*, January, 2007.

[25] E. Josyula and W. F. Bailey, "Governing Equations for Weakly Ionized Plasma Flowfields of Aerospace Vehicles," *Journal of Spacecraft and Rockets*, Vol. 40, No. 6, 2003, pp. 845–857.

[26] M. Fang, Z. Li, Z. Li, and C. Li, "DSMC Approach for Rarefied Air Ionization during Spacecraft Reentry," Vol. 23, No. 4, 2018, pp. 1167–1190.

[27] M. A. Gallis, Chief Author, SPARTA Direct Simulation Monte Carlo (DSMC) Simulator, Sandia National Laboratories, to J.J. Runco, MS Student, Air Force Institute of Technology, E-mail, Subject: Fix Ambipolar Question Response, November, 2018.

[28] A. A. Shevyrin, P. V. Vashchenkov, Y. A. Bondar, and M. S. Ivanov, "Validation of DSMC Results for Chemically Non-equilibrium Air Flows Against Measurements of the Electron Number Density in RAM-C II Flight Experiment," Vol. 1628, 2014, pp. 155–161.

[29] J. D. Anderson Jr., *Hypersonic and High-Temperature Gas Dynamics*, Second Edition. Blacksburg, VA: American Institute of Aeronautics and Astronautics, Inc., 2006.

[30] D. S. K. Reddy and K. Sinha, "Effect of Chemical Reaction Rates on Aeroheating Predictions of Reentry Flows - Version 1," *Journal of Thermophysics and Heat Transfer*, Vol. 25, 2011, pp. 21–33.

[31] D. A. Vallado, *Fundamentals of Astrodynamics and Applications*, Fourth Edition. Hawthorne, CA: Microcosm Press, 2013.

[32] Z. Wu, R. Hu, X. Qu, X. Wang, and Z. Wu, "Space Debris Reentry Analysis Methods and Tools," *Chinese Journal of Aeronautics*, Vol. 24, No. 4, 2011, pp. 387–395.

[33] J. D. Anderson Jr., *Fundamentals of Aerodynamics*, Fifth Edition. New York, NY: McGraw-Hill, 2011.

[34] A. Tewari, "Entry Trajectory Model with Thermomechanical Breakup," *Journal of Spacecraft and Rockets*, Vol. 46, No. 2, 2009, pp. 299–306.